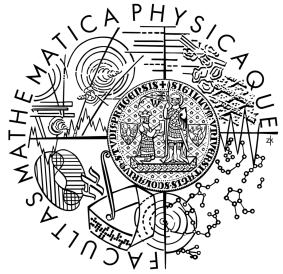

FACULTY
OF MATHEMATICS
AND PHYSICS
Charles University

MASTER THESIS

Patrik Švančara

Visualization of particle motions in superfluid helium flows

Department of Low Temperature Physics

Supervisor of the master thesis:	Dr. Marco La Mantia, Ph.D.
Study programme:	Physics
Study branch:	Physics of Condensed Matter and Materials

Prague 2017

I declare that I carried out this master thesis independently, and only with the cited sources, literature and other professional sources.

I understand that my work relates to the rights and obligations under the Act No. 121/2000 Sb., the Copyright Act, as amended, in particular the fact that the Charles University in Prague has the right to conclude a license agreement on the use of this work as a school work pursuant to Section 60 subsection 1 of the Copyright Act.

In ..... date ..... signature of the author

Title
Visualization of particle motions in superfluid helium flows

Author
Patrik Švančara

Department
Department of Low Temperature Physics

Supervisor
Dr. Marco La Mantia, Ph.D., Department of Low Temperature Physics

Abstract
Flows of normal and superfluid ^{4}He (He I and He II, respectively) are investigated experimentally. Relatively small particles of solid hydrogen and deuterium are suspended in the experimental volume and their motions are tracked in both mechanically and thermally driven flows. A statistical study of the particle velocity and velocity increment distributions is performed at scales smaller and larger than the mean distance between quantized vortices, the quantum length scale of the investigated flows. We show that, at small scales, the observed particle dynamics in He II is greatly influenced by that of quantized vortices. We, additionally, report that this behavior is independent of the imposed large-scale flow. Instead, at large scales, we observe that particle motions are quasiclassical, that is, very similar to those reported to occur in turbulent flows of viscous fluids. The study reinforces therefore the idea of close similarity between viscous flows and large-scale (mechanically-driven) flows of He II, and simultaneously highlights the small-scale differences due to the presence of quantized vortices in He II.

Keywords
low temperature physics • superfluidity • quantum turbulence • flow visualization

I would like to thank my supervisor, Dr. Marco La Mantia, Ph.D., for his excellent guidance when preparing this work. I am also thankful to my consultant, RNDr. Daniel Duda, for his contribution to the performed experiments, and to prof. RNDr. Ladislav Skrbek, DrSc., for many useful comments on the thesis. Finally, I thank my parents for their unlimited support in my studies.

Contents

Preface

The research in the field of low temperature physics begun more than a century ago, when adequate cooling techniques were developed and low enough temperatures were achieved. The first milestone of low temperature physics is considered to be the liquefaction of helium. It was performed by the Dutch physicist Heike Kamerlingh Onnes in 1908 [1]. He achieved temperatures below 2 K. Later, many striking properties of condensed matter were revealed at such low temperatures, e.g., superconductivity, which was also discovered by Onnes in 1911 [2]. But besides the usefulness of liquid helium as a coolant [3], it displays a variety of interesting properties on its own.

For example, the phase diagram of liquid ^{4}He does not contain the triple point, i.e., the point of coexistence of three phases, liquid, solid and gaseous. Moreover, ^{4}He remains liquid in the absolute zero temperature limit, at finite pressure. This behavior is linked with the second-order phase transition that occurs in the liquid phase at $T_\lambda \simeq 2.17\,\mathrm{K}$, at the saturated vapor pressure, called the superfluid transition. The high-temperature, viscous phase of liquid ^{4}He is called He I, and we refer to the superfluid or low-temperature phase as He II.

He II gained the attention of the scientific community for the first time in the 1930's when researchers discovered its non-trivial hydrodynamic and thermodynamic properties. For example, the heat conductivity of He II is orders of magnitude larger than that of He I and in fact the largest among the known materials [4]. Additionally, Kapitza observed that He II can flow through narrow channels without internal friction [5]. This property, i.e., the occurrence of inviscid flows, defines the superfluid nature of He II. But almost simultaneously Andronikashvili reported that torsional oscillations of a pile of thin disks submerged in He II are damped by friction forces due to a non-zero effective viscosity [6]. Other experiments carried out by Allen and Jones [7] revealed that the heat input to the He II bath produces a measurable flow. More specifically, they

observed that temperature gradients in He II induce pressure gradients and thus a flow. These early results indicated indeed that the hydrodynamics of He II is very rich.

The most successful phenomenological model of He II is called the two-fluid model. While the first ideas were reported by Tisza [8], the model was reformulated and completed by Landau [9]. The model is based on the assumption that the flow of He II can be decomposed into the flow of two interpenetrating fluids, the normal fluid and superfluid components. While the normal component is viscous and carries the entire He II entropy, the superfluid component is an inviscid fluid, capable of frictionless flow. Such an approach enabled researchers to clarify various experimental observations. For example, the abnormally large heat conductivity of He II [4] can be explained as the occurence of a thermally driven flow of the normal component without any net mass flow (i.e., the superfluid component flows in the opposite direction).

The loss of viscosity in He II can be interpreted as the localization of a macroscopic amount of helium atoms to their ground state. These atoms display a collective behavior, i.e., they create a macroscopic mass wave, associated with the order parameter $\psi(\mathbf{r}, t)$, a function of position $\mathbf{r}$ and time t. Feynman [10] suggested that one-dimensional singularities of the order parameter, called quantized vortices, can exist in the superfluid component. They greatly influence He II hydrodynamics, because they, for example, determine the small-scale motion of the superfluid component.

The most general form of turbulence in fluids displaying superfluidity is called quantum turbulence [11]. In He II, it occurs at temperatures above 1 K. Research in quantum turbulence is well established as a vivid branch of fluid mechanics and low-temperature physics, including experimental investigation, numerical simulations and theoretical works.

The method we employed for the experimental study of quantum flows is direct flow visualization. It is based on observing the motion of small probes, such as solid particles or bubbles, dispersed in the experimental volume. The probes are usually sensitive to both components of He II, as they interact with the normal component due to viscous drag, but they can also interact with quantized vortices. Experimental data regarding particle dynamics hence provide complex information about both components of He II.

The results we present in this work were obtained from the tracks of small solid particles in He II flows that were generated both mechanically, i.e., by the motion of an obstacle, or thermally, i.e., by a local heat input into the He II bath.

Structure of the thesis

In the first chapter, we explain the underlying physics of the investigated problems. We describe He II from the point of view of quantum mechanics and classical hydrodynamics and we study particle dynamics in He II. In the second chapter, we outline various experimental techniques of flow visualization in superfluids that are accessible by date. We describe our experimental apparatus and relevant data processing techniques in the third chapter. In the fourth chapter we present the obtained experimental results and we provide their interpretation in the scope of present theories. In the fifth chapter we summarize the outcome of the work.

1 Theoretical Part

1.1 Liquid helium and superfluidity

Although helium is the second most abundant element in the Universe after hydrogen, its sources on Earth are scarce. Gaseous helium is usually obtained from natural gas [12].

An atom of ^{4}He consists of two protons and two neutrons that form its nucleus, and a pair of 1s electrons. Therefore, ^{4}He atoms are bosons, while atoms of ^{3}He, another stable helium isotope, are fermions. As a consequence, the low-temperature behavior of ^{3}He significantly differs from that of ^{4}He and is not the subject of this thesis.

The superfluid transition in liquid ^{4}He is linked with its bosonic nature. It is a second-order phase transition and it separates the two liquid phases of ^{4}He called He I (normal phase) and He II (superfluid phase), see dashed line in fig. 1.1. Although the temperature of the transition is slightly pressure-dependent, for practical reasons we refer to the transition temperature as to $T_\lambda \simeq 2.172\,\mathrm{K}$, i.e., its value at the saturated vapor pressure, 37.8 torr [4].

He I, the normal liquid phase, behaves as a viscous fluid of small density, ca. $125\,\mathrm{kg/m^3}$ at 4.2 K, and low kinematic viscosity, of the order of $10^{-8}\,\mathrm{m^2/s}$ [4]. It is a colorless and odorless liquid. Its refractive index is close to unity, therefore one can struggle to observe its surface in a glass vessel. Due to the low value of its specific and latent heat [12], He I can be easily overheated. Bubbles rising from the volume of boiling He I make the observation of the liquid easier.

The superfluid phase is called He II and remains liquid also in the absolute zero limit, i.e., $0\,\mathrm{K} = -273.15\,^\circ\mathrm{C}$, below pressure of 2.5 MPa. Its density and optical properties are not very different from those of He I. Its thermal conductivity is, however, orders of magnitude larger. The existence of thermal inhomogeneities

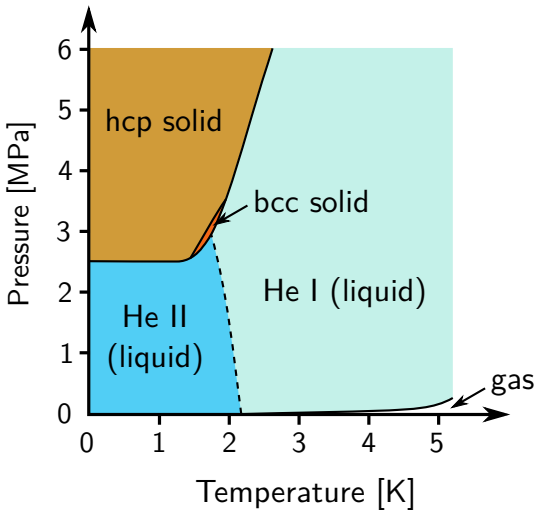

Figure 1.1: Phase diagram of ^{4}He. Note that ^{4}He does not have a triple point, i.e., the point of coexistence of gaseous, liquid and solid phases. Solid helium exists only at increased pressure. The liquid phase can exist also in the zero temperature limit. The phase transition between the normal and superfluid phases (He I and He II, respectively), the lambda-transition, is marked with a dashed line.

in He II is suppressed, which leads to the lack of volume boiling. Superfluid properties of He II include, for example, the occurrence of the two-fluid behavior, the vorticity quantization and various types of flows, some of which have no classical counterparts. We will address these properties in detail below.

The two fluid model

The most successful phenomenological large-scale model of He II is called the two fluid model. The first ideas regarding this model were developed by Tisza in 1938 and the model was completed by Landau in 1941 and 1947 [8, 9]. Several hydrodynamic phenomena occurring in He II can be explained if we look at He II as if it were a system consisting of two interpenetrating fluids, the normal and superfluid components. The density of He II is given as the sum of those of its components, $\varrho_\mathrm{s} + \varrho_\mathrm{n}$, where subscripts "s" and "n" represent the superfluid and normal components, respectively. Although the total He II density, ϱ, does not vary much with temperature, the respective densities of the components are strongly temperature dependent, see fig. 1.2. At T_λ, just below the superfluid transition, there is only the normal component present. But at lower temperatures, the density of the normal component quickly decreases, while that of the superfluid component rises.

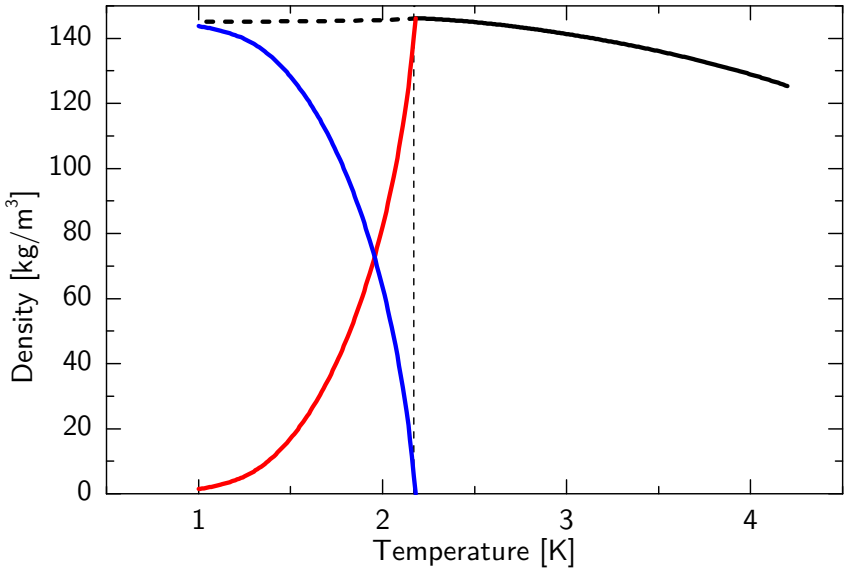

Figure 1.2: The density of liquid ^{4}He as a function of temperature. The black lines denote the density of He I (solid line) and the combined density of the normal and superfluid components of He II (dashed line). The densities of the normal and superfluid components of He II are denoted by the red and blue lines, respectively. Relevant data values are obtained from [13].

The normal component of He II is represented as a gas of thermal excitations or quasiparticles. The heat and momentum transfer in He II is allowed by quasiparticle emissions and absorptions. The normal component has therefore nonzero entropy and viscosity.

The superfluid component instead represents the microscopically coherent part of He II. Such a system, localized in the ground state, in momentum space, has zero entropy and viscosity.

Macroscopically, one can define two velocity fields in He II: $\mathbf{v}_\mathrm{n}$ and $\mathbf{v}_\mathrm{s}$, for the normal and superfluid components, respectively. The incompressibility condition for He II can be written, for a constant temperature, as

$$\frac{\partial \varrho}{\partial t} + \nabla \cdot (\varrho_\mathrm{n}\mathbf{v}_\mathrm{n} + \varrho_\mathrm{s}\mathbf{v}_\mathrm{s}) = 0. \tag{1.1}$$

In the equation $\varrho = \varrho_\mathrm{n} + \varrho_\mathrm{s}$ denotes the total density of He II.

Two equations of motion have to be written for He II. The viscous normal component can be described by the incompressible Navier-Stokes equation. On the other hand, the Euler equation for ideal fluids is more appropriate for the inviscid superfluid component. Moreover, we must take into account the mutual

interaction between the components that couples them together. The final form of the equations of motion is, in the case of incompressible flow, for the normal component [3]

$$\varrho_{\mathrm{n}}\frac{\partial \mathbf{v}_{\mathrm{n}}}{\partial t} + \varrho_{\mathrm{n}}(\mathbf{v}_{\mathrm{n}}\cdot\nabla)\mathbf{v}_{\mathrm{n}} = -\frac{\varrho_{\mathrm{n}}}{\varrho}\nabla p - \varrho_{\mathrm{s}}S\nabla T + \mathbf{F}_{\mathrm{ns}} + \mu\nabla^2\mathbf{v}_{\mathrm{n}}, \tag{1.2}$$

and for the superfluid component

$$\varrho_{\mathrm{s}}\frac{\partial \mathbf{v}_{\mathrm{s}}}{\partial t} + \varrho_{\mathrm{s}}(\mathbf{v}_{\mathrm{s}}\cdot\nabla)\mathbf{v}_{\mathrm{s}} = -\frac{\varrho_{\mathrm{s}}}{\varrho}\nabla p + \varrho_{\mathrm{s}}S\nabla T - \mathbf{F}_{\mathrm{ns}}. \tag{1.3}$$

In the equations above, ∇p indicates the pressure gradient, S is the entropy of He II per unit mass and ∇T represents the temperature gradient. $\mathbf{F}_{\mathrm{ns}}$ denotes the force of mutual friction, i.e., the coupling term between the components. Note that $\mathbf{F}_{\mathrm{ns}}$ has opposite signs in equations (1.2) and (1.3). Finally, μ is dynamic viscosity of the normal component that is tabulated, as well as the He II specific entropy in [4].

The terms proportional to the thermal gradient ∇T are also of opposite signs. As a consequence, any flow induced by local heat sources, such as resistive heaters, will produce the flow of the normal component away from the heater and the flow of the superfluid component towards the heater. We call this flow type thermal counterflow. The use of thermal counterflow in He II research is frequent, because such flow has no obvious classical counterpart in viscous liquids and is easy to obtain. The relative velocity of the components is, in the simple case of a channel that is closed at one end and open at the other, with a flat heater at the closed channel end [11],

$$v_{\mathrm{ns}} = |v_{\mathrm{n}} - v_{\mathrm{s}}| = \frac{\dot{q}}{\varrho_{\mathrm{s}}ST}, \tag{1.4}$$

where $\dot{q}$ indicates the heat flux supplied to the channel.

Quantized vortices

The superfluid component displays a collective behavior, which leads to all the phenomena listed above. To describe such a state, we can use the order parameter $\psi(\mathbf{r}, t)$, a function of space coordinate $\mathbf{r}$ and time t. From the point of view of quantum mechanics, we can associate ψ with the macroscopic wave function of the superfluid component. The complex function ψ can be decomposed to its

amplitude $|\psi(\mathbf{r},t)|$ and phase $\phi(\mathbf{r},t)$:

$$\psi(\mathbf{r},t) = |\psi(\mathbf{r},t)|\mathrm{e}^{\mathrm{i}\phi(\mathbf{r},t)}. \tag{1.5}$$

The square of the amplitude represents the probability of finding a ^{4}He atom in a unitary volume. In the case of He II, we can identify this quantity with the density of the superfluid component, i.e.,

$$|\psi|^2 = \varrho_\mathrm{s} \quad \Rightarrow \quad |\psi| = \sqrt{\varrho_\mathrm{s}}. \tag{1.6}$$

The phase ϕ of the macroscopic wave function influences the resulting hydrodynamics of the superfluid component. We can calculate its velocity as $\mathbf{v}_\mathrm{s} = \mathbf{p}_\mathrm{s}/m_4$, where m_4 is the mass of a ^{4}He atom and $\mathbf{p}_\mathrm{s}$ indicates the eigenvalue of the momentum operator $\hat{\mathbf{p}} = -\mathrm{i}\hbar\nabla$:

$$\hat{\mathbf{p}}\psi = -\mathrm{i}\hbar\nabla\left(|\psi|\mathrm{e}^{\mathrm{i}\phi}\right) = -\mathrm{i}\hbar|\psi|\nabla\left(e^{\mathrm{i}\phi}\right) = \hbar\psi\nabla\phi \quad \Rightarrow \quad \mathbf{p}_\mathrm{s} = \hbar\nabla\phi. \tag{1.7}$$

We get therefore that $\mathbf{v}_\mathrm{s}$ is proportional to the gradient of the phase ϕ

$$\mathbf{v}_\mathrm{s} = \frac{\mathbf{p}_\mathrm{s}}{m_4} = \frac{\hbar}{m_4}\nabla\phi. \tag{1.8}$$

A velocity field that is obtained as the gradient of a scalar function is called potential. The corresponding flow has no vorticity $\boldsymbol{\omega}_\mathrm{s} = \nabla \times \mathbf{v}_\mathrm{s}$, since the curl of any gradient is identically zero.

Experimental observations of rotating He II, which mimics the rotation of a solid body, showed that the flow of the superfluid component can be of non-zero vorticity. In consequence, Feynman and Onsager [10, 14] introduced one-dimensional topological defects that occur in the superfluid component, called quantized vortices, to explain the experimental findings. The vortices have a few ångstrom in size, their cores do not contain the superfluid component and break the volume of He II into multiply connected domains. Possible values of circulation Γ of the superfluid component along an arbitrary closed curve $\partial\Omega$ are given as a spectrum of discrete values

$$\Gamma[\partial\Omega] = \oint_{\partial\Omega} \mathbf{v}_\mathrm{s} \cdot \mathrm{d}\boldsymbol{\ell} = 2\pi n\frac{\hbar}{m_4} = n\kappa, \tag{1.9}$$

where n is a non-zero positive integer and $\kappa = h/m_4 = 9.97 \times 10^{-8}\,\mathrm{m}^2/\mathrm{s}$ denotes the quantum of circulation [15].

Consider, for the sake of simplicity, a straight, singly quantized vortex in the vertical direction, of infinite length in an infinite tank of He II. Due to the translation symmetry along the vortex line, steady flow of the superfluid component must be zero in the vertical coordinate, and due to the mass conservation law the radial component has to be zero, too. In consequence, only the tangential component of $\mathbf{v}_\mathrm{s}$ is nonzero and, due to the symmetry of the problem, depends only on the distance from the vortex core r. We can hence write, in cylindrical coordinates, $\mathbf{v}_\mathrm{s} = (0, v_\mathrm{s}(r), 0)$.

If we calculate the circulation Γ along a circle $\mathcal{C}_r$ of radius r, we get for this geometry

$$\Gamma[\mathcal{C}_r] = \oint_{\mathcal{C}_r} \mathbf{v}_\mathrm{s} \cdot \mathrm{d}\boldsymbol{\ell} = v_\mathrm{s}(r) 2\pi r. \tag{1.10}$$

However, from eq. (1.9), the value of Γ is independent of the integration path and equal to κ. Hence we get for the velocity field around a vortex

$$v_\mathrm{s}(r) 2\pi r = \kappa \quad \Rightarrow \quad v_\mathrm{s}(r) = \frac{\kappa}{2\pi r}. \tag{1.11}$$

The obvious divergence of v_s as $r \to 0$ is compensated by the drop of the density of the superfluid component in the vortex core. In other words, approaching to the vortex core, which is roughly $\xi \simeq 10\,\mathrm{nm}$ thick [16], leads to the local loss of superfluidity, see fig. 1.3.

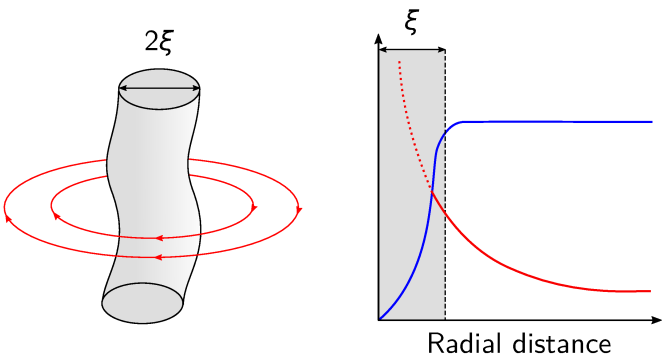

Figure 1.3: Left: Scheme of a quantized vortex. The red lines illustrate the velocity field of the superfliud component. Right: Structure of a quantized vortex as a function of radial distance from its core. The red line indicates the radial profile of $\mathbf{v}_\mathrm{s}$, while the blue line denotes the density of the superfluid component.

A more realistic model of a single rectilinear vortex constrains the vortex in the space between ξ, the vortex core radius, and R, the size of a finite tank containing the liquid. We now consider a general value of circulation $n\kappa$, for $n \geq 1$. If we

assume that the density ϱ_s is constant in the range of possible radial distances, we can directly calculate the kinetic energy of the superfluid component per unit vortex length as

$$\varepsilon = \int_\xi^R \frac{1}{2}\varrho_\mathrm{s} v_\mathrm{s}^2 2\pi r \mathrm{d}r = \frac{n^2\kappa^2\varrho_\mathrm{s}}{4\pi}\int_\xi^R \frac{\mathrm{d}r}{r} = \frac{n^2\kappa^2\varrho_\mathrm{s}}{4\pi}\ln\left(\frac{R}{\xi}\right). \tag{1.12}$$

The energy ε is proportional to n^2, which means, for example, that the combined energy of two singly quantized vortices is smaller compared to the energy of one vortex for which $n = 2$. Therefore, from the principle of minimum energy follows that all the vortices in He II are singly quantized. This result is also supported by experiments [15]. In order to quantify the amount of quantized vortices in He II, it is necessary only to measure their total length per unit volume. We call this quantity the vortex line density L.

Quantized vortices exist in the form of closed loops, called vortex rings, or as vortex lines. However, these lines cannot be open inside the He II volume: they must be pinned to the container walls or end on the liquid surface. On the other hand, they are allowed to bend, stretch, and reconnect. In consequence, the vortex line density can vary in time. Besides the superfluid component, the dynamics of quantized vortices is influenced also by the normal component via the scattering of thermal quasiparticle excitations. This opens a channel for mutual interaction, denoted by the force of mutual friction $\mathbf{F}_\mathrm{ns}$, see eq. (1.2) and (1.3), between the normal and superfluid components [17]. Due to these interactions, quantized vortices tend to create a dense vortex tangle, the main ingredient of quantum turbulence.

1.2 Quantum and classical turbulence

Turbulence in He II, at temperatures above 1 K, includes, in its most general form, turbulence in the normal component, the flow of the superfluid component and their interactions with the dynamics of the vortex tangle. The most striking feature of the turbulent vortex tangle is that it includes only monodisperse, singly quantized vortices, while the size distribution of turbulent eddies in viscous flows is instead continuous.

Dynamics of vortex tangle

As we have already mentioned, quantized vortices can exist in He II in form of rings or lines. Propagating quasiparticle excitations often interact with the vortices, which leads to reconnections of the vortex lines. As a result, the total vortex line density L increases until a steady state is reached, accordingly to the relevant flow forcing. Possible flow generators that can trigger the increase of vortex line density in He II include heaters for thermal counterflow or mechanical generators commonly used in classical turbulence, e.g., moving grids or various propellers.

When the flow forcing is switched off, the vortex line density follows a transient and eventually decreases. Note that the quiescent He II is not vortex-free, some quantized vortices are always preserved; they are called the remnant vortices. Both the steady-state and decaying vortex tangle are subject to vivid scientific research by various numerical and experimental methods [18].

Classical turbulence

The nature of turbulence in viscous fluids can be often characterized, for example, by a non dimensional parameter, introduced for the first time by Reynolds, defined as the ratio of inertial to viscous forces in the flow:

$$\mathrm{Re} = \frac{VD}{\nu}, \tag{1.13}$$

where V denotes a characteristic flow velocity, D indicates a characteristic flow scale and ν is the kinematic viscosity of the fluid. Turbulent instabilities are linked with large values of Re, while small values of Re indicate a strong influence of viscous forces and subsequent energy dissipation.

In tridimensional turbulent flows, dissipation occurs often at small scales, i.e., for small D, when $\mathrm{Re} \simeq 1$. As a consequence, the kinetic energy of the flow is transferred between scales towards the smaller ones, at which viscous forces dominante and effectively dissipate the energy. This small scale is called the Kolmogorov dissipative scale η [19]. It is customary to express the length scales, or size of turbulent eddies, in the space of wave numbers (k-space). Small scales are therefore represented by large k values, i.e., in steady-state turbulence, energy that enters the system at small values of k must be transferred towards larger

k at a constant rate ϵ. The energy transfer is governed by inertial forces and dissipate very little energy [20].

The Kolmogorov length scale depends, under the assumption of the small-scale self similarity of turbulence [19], only on the kinematic viscosity of the fluid and the energy transfer rate as

$$\eta = (\nu^3/\epsilon)^{1/4}. \tag{1.14}$$

If the Reynolds number of the flow of He II is large enough, classical turbulence can occur in the normal component. If this is the case, He II provides a complex turbulent system that consists of two coupled turbulent components. Strikingly, the resulting physical picture is quite similar to the classical one. For example, Maurer and Tabeling [21] reported that the measured energy spectra of turbulence in He I and in He II are indistinguishable. However, some differences can be observed as well. Visualization of mechanically driven flows in liquid helium [22] showed that the strength of macroscopic vortices shed by an oscillating cylinder is qualitatively different in He I and in He II, at small scales.

1.3 Particle dynamics in ^{4}He flows

In most cases, flow visualization techniques require to suspend solid particles into the fluid to track the investigated flow. Therefore, we have to study the forces acting on the particles and understand to what extent the particles are able to faithfully track various flows. The analysis of the forces acting on a particle is notably important in He II, where the motions of particles are influenced by the normal and superfluid components at the same time, alongside with their interactions with quantized vortices.

Hydrodynamic forces and particle equation of motion

According to Poole et al. [23], we will consider spherical particles, of radius a and density ϱ_p. In the following equations we denote the velocity of a particle as $\mathbf{u}$. Firstly, we neglect interactions with quantized vortex lines. We also assume that the particles are smaller than the relevant Kolmogorov length η.

The dominant force that the normal component flow generates on a particle is the viscous drag. In the case of small Reynolds numbers, the force scales linearly

with the velocity of the particle $\mathbf{u}$ relative to that of the normal component $\mathbf{v}_\mathrm{n}$:

$$\mathbf{F}_\mathrm{d} = 6\pi a \mu_\mathrm{n} (\mathbf{v}_\mathrm{n} - \mathbf{u}). \tag{1.15}$$

This formula is correct only when the gas of quasiparticles, representing the normal component, can be considered as a continuum, i.e., the mean free path of a quasiparticle is less than the typical particle size (that is of the order of 1 μm for typical experiments). Due to the temperature dependence of the mean free path, this condition is safely fulfilled for $T > 1\,\mathrm{K}$ [23].

For a particle whose density does not match that of the fluid, which is usually the case in experiments, the combined forces of gravity and buoyancy are nonzero and equal to

$$\mathbf{F}_g = V(\varrho_\mathrm{p} - \varrho)\mathbf{g}, \tag{1.16}$$

where $V = 4\pi a^3/3$ denotes the particle volume and $\mathbf{g}$ indicates the acceleration due to gravity.

The fluid that accelerates around the particles creates an additional inertial force

$$\mathbf{F}_\mathrm{i} = \varrho V \frac{\mathrm{D}\mathbf{v}}{\mathrm{D}t}, \tag{1.17}$$

where $\mathrm{D}/\mathrm{D}t$ denotes the operator of material (substantial) derivative

$$\frac{\mathrm{D}}{\mathrm{D}t} = \frac{\partial}{\partial t} + \mathbf{v} \cdot \nabla. \tag{1.18}$$

The added mass force, due to the acceleration of a particle embedded in the fluid, can be expressed as

$$\mathbf{F}_\mathrm{am} = C\varrho V \left(\frac{\mathrm{D}\mathbf{v}}{\mathrm{D}t} - \frac{\mathrm{d}\mathbf{u}}{\mathrm{d}t} \right), \tag{1.19}$$

where C is the added mass coefficient ($C = 1/2$ for spherical particles). Note that eq. (1.17) and (1.19) are valid for both the normal and superfluid components, i.e., one can use $\mathbf{v}_\mathrm{n}$ or $\mathbf{v}_\mathrm{s}$ instead of $\mathbf{v}$ and ϱ_n or ϱ_s instead of ϱ, respectively.

Other hydrodynamic forces due to the flow history, particle rotation, etc. can be neglected if the particles are small enough compared to the smallest scale of turbulence, which is usually the case [23]. We can hence write the equation of

motion for a single particle in He II

$$\varrho_{\mathrm{p}} V \frac{\mathrm{d}\mathbf{u}}{\mathrm{d}t} = 6\pi a \mu_{\mathrm{n}} (\mathbf{v}_{\mathrm{n}} - \mathbf{u}) + V(\varrho_{\mathrm{p}} - \varrho)\mathbf{g} + \\ + \varrho_{\mathrm{n}} V \frac{\mathrm{D}\mathbf{v}_{\mathrm{n}}}{\mathrm{D}t} + C\varrho_{\mathrm{n}} V \left(\frac{\mathrm{D}\mathbf{v}_{\mathrm{n}}}{\mathrm{D}t} - \frac{\mathrm{d}\mathbf{u}}{\mathrm{d}t} \right) + \\ + \varrho_{\mathrm{s}} V \frac{\mathrm{D}\mathbf{v}_{\mathrm{s}}}{\mathrm{D}t} + C\varrho_{\mathrm{s}} V \left(\frac{\mathrm{D}\mathbf{v}_{\mathrm{s}}}{\mathrm{D}t} - \frac{\mathrm{d}\mathbf{u}}{\mathrm{d}t} \right). \quad (1.20)$$

This equation can be simplified, for neutrally buoyant (i.e., $\mathbf{F}_g = 0$) and spherical ($C = 1/2$) particles, to the form

$$\frac{\mathrm{d}\mathbf{u}}{\mathrm{d}t} = \frac{1}{\tau}(\mathbf{v}_{\mathrm{n}} - \mathbf{u}) + \frac{1}{\varrho} \left(\varrho_{\mathrm{n}} \frac{\mathrm{D}\mathbf{v}_{\mathrm{n}}}{\mathrm{D}t} + \varrho_{\mathrm{s}} \frac{\mathrm{D}\mathbf{v}_{\mathrm{s}}}{\mathrm{D}t} \right), \quad (1.21)$$

where $\varrho = \varrho_{\mathrm{n}} + \varrho_{\mathrm{s}}$ and τ is defined as

$$\tau = \frac{\varrho a^2}{3\mu_{\mathrm{n}}} \quad (1.22)$$

and represents the characteristic response time of a particle to the flow variations.

Interactions between particles and quantized vortices

Quantized vortices in He II can influence the motion of suspended particles, provided that the particles are small enough to react on their presence in He II. We will illustrate the underlying physics in the case of a neutrally buoyant spherical particle in the vicinity of one straight vortex. If we neglect the influence of the particle on the vortex line, the imposed velocity field $\mathbf{v}_{\mathrm{s}}$ is, in the cylindrical coordinate system, $\mathbf{v}_{\mathrm{s}} = (0, \kappa/(2\pi r), 0)$, see eq. (1.11). For the sake of simplicity, we assume that the normal component is at rest, i.e., $\mathbf{v}_{\mathrm{n}} = 0$. Under these assumptions, the relevant equation of motion can be derived from eq. (1.20):

$$\frac{\mathrm{d}\mathbf{u}}{\mathrm{d}t} = -\frac{1}{\tau}\mathbf{u} + \frac{\varrho_{\mathrm{s}}}{\varrho}(\mathbf{v}_{\mathrm{s}} \cdot \nabla)\mathbf{v}_{\mathrm{s}}. \quad (1.23)$$

The last term on the right hand side of the equation above has only a radial component other than zero and can be expressed as

$$(\mathbf{v}_{\mathrm{s}} \cdot \nabla)\mathbf{v}_{\mathrm{s}} = \frac{1}{2}\nabla(\mathbf{v}_{\mathrm{s}}{}^2) = \frac{\kappa^2}{8\pi^2}\nabla\left(\frac{1}{r^2}\right). \quad (1.24)$$

Due to this term, the particle is attracted towards the vortex line and starts to move radially from its initial position. The motion is governed by the equation

$$\frac{\mathrm{d}u}{\mathrm{d}t} = -\frac{u}{\tau} - \frac{2\beta}{r^3}, \tag{1.25}$$

where $\beta = \varrho_\mathrm{s}\kappa^2/(8\pi^2\varrho)$ is a scaling factor dependent on temperature. We can solve this equation numerically or we can calculate its approximative solution analytically. Following [23], we can argue that the left hand side of eq. (1.25), i.e., the particle acceleration, is negligibly small compared to the right hand side, when the particle is far away from the vortex core. Therefore, we can set the acceleration to be zero, which leads us to an equation that can be solved by variable separation. The resulting solution is

$$r(t) = \left(r_0^4 - 8\beta\tau t\right)^{1/4}, \tag{1.26}$$

where r_0 is the original position of the particle at $t = 0$. The second derivative of this equation yields the acceleration that is proportional to $(\beta\tau)^2$. For micron-sized particles, suspended in He II, the value of this factor is as low as $10^{-42}\,\mathrm{m}^8/\mathrm{s}^4$ and the acceleration can be indeed neglected.

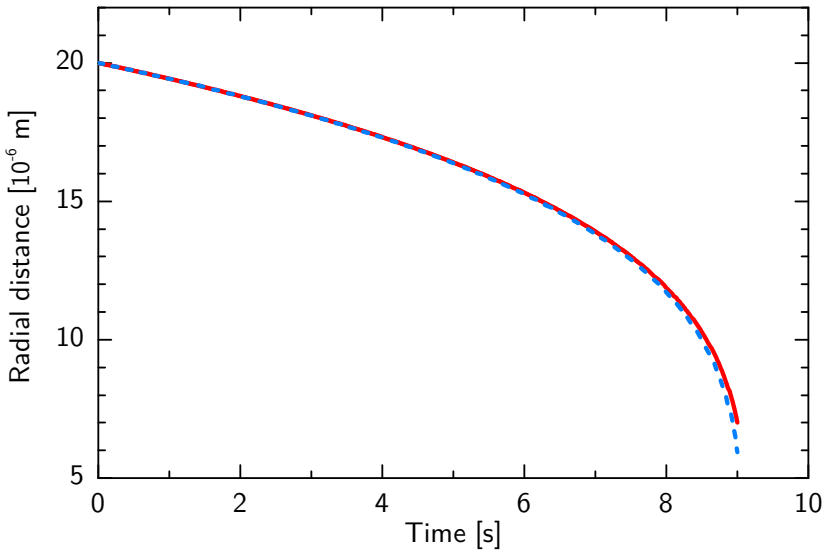

Figure 1.4: Attraction of a particle by a straight infinite vortex line, located at $r = 0$. The considered particle is neutrally buoyant, of 1 µm radius and originally put in rest at 20 µm away from the vortex. The temperature of the He II bath is chosen to be 1.95 K when He II contains the same amount of the normal and superfluid components. The red solid line represents the approximate analytical solution (1.26), the blue dashed line indicates the numerical solution of particle equation of motion (1.25) performed by the lsode solver in the Octave environment.

In fig. 1.4, we plot the function $r(t)$ according to eq. (1.26) and the numerical solution of eq. (1.25) for neutrally buoyant spherical particles of 1 μm diameter, suspended in He II at 1.95 K. We can observe that the exact and approximate solutions do not differ when the particle is located relatively far away from the vortex line (ca. 10 μm). However, nonzero particle acceleration becomes important when the particle gets close enough.

Moreover, when the particle is too close to the vortex, the model described above becomes insufficient and one has to consider that the particle affects the geometry of the vortex [23]. More specifically, the vortex becomes curved and starts to move. Eventually, the particle approaches the vortex with a finite velocity and, if this velocity is not too large, becomes trapped on the vortex line, see fig. 1.5.

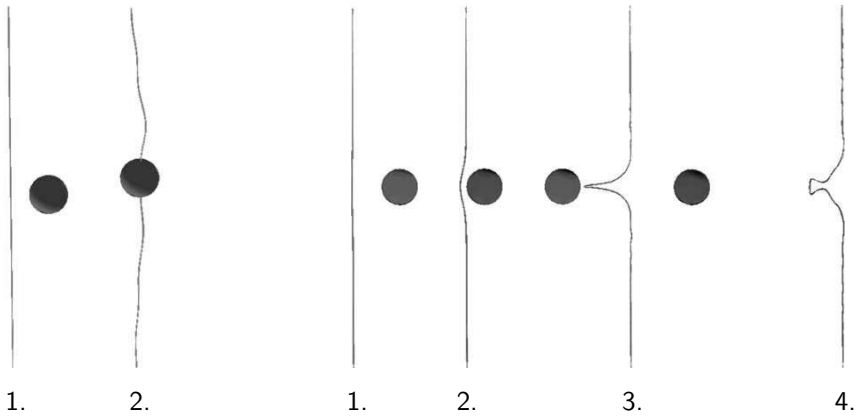

Figure 1.5: Interaction between a quantized vortex and a solid particle. Left: particle approaches the vortex line, which becomes deformed and, eventually, the particle gets trapped. Right: particle approaches the vortex, gets trapped but instantly de-traps and excites waves along the vortex line. Image from [16], reprinted with permission from Elsevier.

Particle trapping is energetically favorable, because a trapping event releases the energy equal to the kinetic energy of the superfluid component, replaced by the trapped particle. For a particle of radius a and a vortex line of core radius ξ, this energy is approximately [16]

$$\Delta E \simeq \frac{\varrho_s \kappa^2 a}{4\pi} \ln\left(\frac{a}{\xi}\right). \tag{1.27}$$

Consequently, ΔE represents the relevant de-trapping energy the particle must obtain in order to be released from the vortex line.

Quantized vortices, decorated with sub-micron particles trapped onto them, were already observed experimentally, see, e.g., [24]. Trapping and de-trapping events represent another feature of particle dynamics in He II flows that can be observed experimentally.

2 Experimental Techniques

Flow visualization techniques are well developed and of great precision in classical fluid dynamics. Many different experimental techniques are applicable to date, for example ink and smoke visualization, hydrogen bubbles, Baker's pH technique, hot wire anemometry, laser Doppler anemometry, particle image velocimetry or particle tracking velocimetry [25, 26].

However, in order to visualize the flows of He II, the experimentalists have to face serious technical challenges. The low-temperature vessel containing liquid helium must be well insulated, therefore the optical access to the experimental volume is usually significantly restrained. Low density and viscosity of He II put another barrier for the use of standard methods, especially regarding the use of tracer particles that will faithfully probe the imposed flows.

Nonetheless, various experimental techniques are available to date [16, 26]. Here we provide a short review on available techniques, but we mainly focus on the particle tracking velocimetry technique that was used by us.

2.1 Microscopic tracers and relevant techniques

There are several efforts to produce microscopic tracer particles in He II. These nonintruisive probes faithfully track the imposed flows. Possible tracers include ^{3}He atoms that are visualized by means of neutron absorption tomography, positively and negatively charged ions and metastable He_2^* molecules [26].

A positive ion in He II attracts nearby helium atoms that agglomerate and compress around the ion. The increase of pressure usually leads to the local solidification and creation of solid helium particles of a few nm in diameter. Contrarily, negative ions (or electrons) repel helium atoms and, consequently, they form bubbles of a few nm diameter [16, 27]. While positively charged particles seem to

follow the normal component of He II, negative bubbles are likely to get trapped on quantized vortices and slide along their length [28].

The use of excimer He_2^* molecules is a relatively new technique [29]. The molecules are created by a series of femtosecond laser pulses in a line ca. 100 µm thick. The mean lifetime of He_2^* excimers is ca. 13 s and their diameter is ca. 6 Å. Usually, the image of the line is collected, by laser-induced fluorescence, after a given time since its creation. Deformations of the line serve to observe the imposed channel flows, such as thermal counterflow [30], see fig. 2.1.

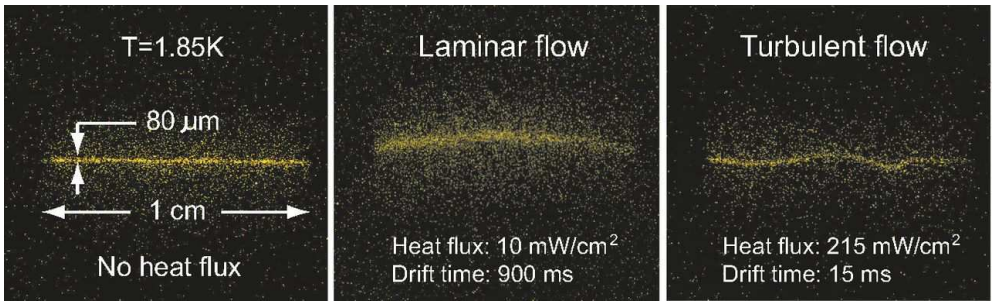

Figure 2.1: Visualization of a line of excimer He_2^* molecules by laser-induced fluorescence. Left: line of excimers in a quiescent flow. Center and right: images of the line distorted by thermal counterflow in laminar and turbulent regimes of the normal component. Image from [26].

2.2 Solid particles and relevant techniques

Other techniques are based on the injection of solid particles into the experimental volume. These particles are larger than the microscopic tracers described above and their positions can be captured optically, e.g., by a high-speed camera. The available experimental techniques are able to follow the motion of a single particle and deduce its velocity (laser Doppler velocimetry), capture many particles at once (particle image velocimetry) or track individual particles in the field of view (particle tracking velocimetry).

Requirements on particle properties

We impose several criteria on particle physical properties in order to faithfully track the investigated flow. Generally, the particles used to seed the flow should be such that they do not disturb the imposed flow, can properly react to turbulent

variations and be easily detected in the experimental volume. According to Van Sciver and Barenghi [16], one has to take into account particle density, size, and its ability to scatter light and not to agglomerate.

Particle density

The buoyancy force (see eq. (1.16)) acting on the particles is proportional to the difference between the densities of the particles and that of liquid helium ($\varrho \simeq 145\,\mathrm{kg/m^3}$, in the superfluid phase [4]), and null for neutrally buoyant particles, i.e., those whose density matches ϱ.

However, the production of neutrally buoyant particles is extremely challenging and, usually, there is a mismatch between the densities. Consequently, one has to consider particle settling. Assuming laminar regime and spherical particles of density ϱ_p, the terminal velocity $\mathbf{u}_\infty$ of particle settling results from the balance between the buoyancy force (1.16) and the Stokes drag (1.15):

$$\mathbf{u}_\infty = \frac{2a^2\mathbf{g}(\varrho_\mathrm{p} - \varrho)}{9\mu}, \tag{2.1}$$

where μ denotes the dynamic viscosity of He II tabulated in [4]. Light particles, i.e., those with $\varrho_\mathrm{p} < \varrho$, raise towards the liquid surface, while heavy particles ($\varrho_\mathrm{p} > \varrho$) sink to the bottom of the vessel. For typical particles used in He II experiments, acceptable settling velocities are of the order of few mm/s, at most. From the practical point of view, particle settling velocity should not overcome few per cents of the typical flow velocity.

Although particle settling is considered to be a parasitic effect, it might be sometimes useful. The velocity $\mathbf{u}_\infty$ is dependent, besides some physical constants, on the particle radius a only. The measurement of the settling velocity can hence be used to estimate the size of the particles. Moreover, these particles gradually leave the experimental field of view, which means that the experimentalists have to periodically re-seed the flow. It also means that the visualized particles are being constantly renewed, which can improve their quality.

Particle size

There are several restrictions imposed on the particle size, especially related to their inertia and ability to respond to the flow variations. We can describe this

ability by particle relaxation time τ, see eq. (1.22), that is, for spherical and neutrally buoyant particles, equal to [16]

$$\tau = \frac{\varrho a^2}{3\mu_\mathrm{n}} = \frac{a^2}{3\nu}, \tag{2.2}$$

where $\nu = \mu_\mathrm{n}/\varrho$ is the kinematic viscosity of the normal component of He II. In order to track fine turbulent variations, particles should be small enough (note that τ scales as $\tau \sim a^2$) so that their relaxation time would be smaller than or equal to the characteristic time scale of the imposed flow. Such a time scale is called the Kolmogorov time and is defined as $\tau_\eta = (\nu/\epsilon)^{1/2}$, where ϵ denotes the mean energy dissipation rate [31]. From the condition $\tau \leq \tau_\eta$ we get

$$a \leq \left(\frac{81\nu^3}{4\epsilon}\right)^{1/4}. \tag{2.3}$$

Additionally, the particle size sets a limit on the resolution of the applied method. Besides the inertial effects described above, the particles should also be smaller than the characteristic small scale of the flow. For the viscous normal component one can define the Kolmogorov length scale [31] $\eta = (\nu^3/\epsilon)^{1/4}$, which poses more severe limit on particle size than eq. (2.3) by a factor of $(81/4)^{1/4} \simeq 2.1$.

Moreover, another length scale arises from vortex dynamics, namely the intervortex distance $\ell \simeq L^{-1/2}$ (L denotes the vortex line density) and represents the mean distance between neighboring vortices. This scale separates different regimes of particle interactions with the vortices and greatly influence the resulting particle motions, as we describe in the following.

Light scattering

Sufficient intensity of the scattered light limits, contrarily to the requirements above, the minimum particle size. Again, according to [16], particles should be at least twice as big as the wavelength of the light used to illuminate the experimental volume. Since most of the methods uses visible light, i.e., the relevant wavelength is $\lambda \simeq 500\,\mathrm{nm}$, this sets the lower limit on particle size as $a > 1\,\mu\mathrm{m}$. Note that the scattered light intensity scales with particle size approximately as a^3 [16].

In conclusion, the micron-sized particles meet, at least to a certain extent, all the criteria listed above. For a typical experiment in He II, $\eta \simeq \ell \geq 1\,\mu\text{m}$ and typical velocities of seeding particles are of the order of a few mm/s.

Particle seeding techniques

Many different particles can be purchased, in a wide range of sizes and densities. For example, hollow glass microspheres can be obtained with density close to that of He II [16], but their diameter ranges from 10 µm to 100 µm with wide size distribution. As a result, their use in visualization studies is scarce. For example, Donnelly et al. [32] used smaller (less than 10 µm in diameter) but heavier glass spheres to study grid flows in He II.

Zhang et al. [33] used, for their visualization studies, small polystyrene spheres. Despite their high density (ca. $1\,000\,\text{kg/m}^3$), they can be obtained with diameter of 1.7 µm and narrow size distribution. This results into relatively small and uniform settling velocity, ca. 0.5 mm/s, that can be taken into account as a constant correction of the measured vertical velocity.

Commercially available fluorescent nanospheres were used recently by Meichle and Lathrop [34]. These particles are of sub-micron size and, consequently, do not rely on light scattering. Instead, they can be visualized by laser-induced fluorescence and they provide better signal-to-noise ratio than other seeding techniques. The method of nanoparticle seeding is already in use to visualize turbulent flows of He II.

Another widely used seeding technique, is based on solidification of various gases in the bath of liquid helium. First attempts in this field were carried out by Chopra and Brown [35]. They used a mixture of gaseous hydrogen and deuterium and they obtained solid particles smaller than 1 mm. Other experimentalits improved this technique, in order to obtain hydrogen or deuterium particles of diameters between 1 µm and 10 µm, see, e.g. [36, 37] with narrow size distributions. Besides hydrogen and deuterium, particles can be obtained by solidification of neon [38] (particles smaller than 10 µm) or air [39] (sub-micron particles that are used mainly to decorate quantized vortices and study their dynamics [24]).

The usual procedure to obtain solid particles is as follows. The seeding gas is firstly diluted with gaseous helium and then pressurized to a defined pressure difference relative to the liquid helium vessel. The gaseous mixture is then injected

in He I (at temperature of ca. 2.2 K) in a series of short pulses of a few ms in length. Since the melting temperature of the seeding gas exceeds that of liquid helium, the diluted gas desublimates in form of small particles, see fig. 2.2.

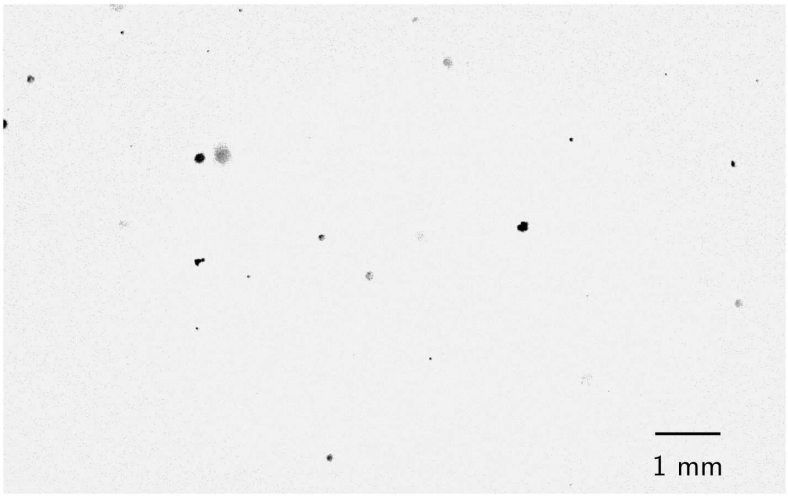

Figure 2.2: Snapshot of the visualization field of view, containing solid deuterium particles suspended in He II, at 1.75 K. Colors are inverted for convenience.

Due to the density mismatch, the particles made of deuterium, neon and air settle towards the bottom of the experimental volume, while hydrogen particles tend to float on the liquid surface. However, due to the relatively narrow size distribution of the particles and moderately slow settling velocities, their use in visualization studies is possible. Attempts to provide neutrally buoyant particles made of a mixture of hydrogen and deuterium failed due to different melting temperatures (14 K and 19 K, for hydrogen and deuterium, respectively) [37]. A more promising option is the use of solid deuterium hydride (HD), in which hydrogen and deuterium atoms are bound in molecules. Detailed study of the compound's potential is yet to be done.

We observed experimentally that solidified particles slowly coalesce, but more detailed explanation of this phenomenon is yet to be done. While hydrogen particles seem to create filaments, deuterium ones agglomerate in form of spherical clusters [37]. Both structures are, however, unsuitable for experimental observation, but settle relatively quickly. However, the progressive deterioration of particle quality limits the duration of one experiment to two or three days. After that, the helium cryostat must be warmed to room temperature and evacuated to remove residual seeding gases.

Particle image velocimetry

The main goal of the particle image velocimetry technique (PIV) is to obtain the velocity field in the entire region of interest at once. The visualized experimental volume is illuminated by a thin laser sheet, where densely seeded particles scatter the incident light. However, the concentration of seeding particles must not be too high in order not to influence the investigated flow. The obtained signal is acquired, perpendicularly to the laser sheet, by a fast camera in pairs of two-dimensional images with well-defined time gap, determined, for example, by the frequency of the laser light pulses.

Later, pairs of images are analyzed. Firstly, the images are split into small interrogation regions containing ca. 15 particles per region [16]. Then, a cross-correlation algorithm is used to compare the mean brightness of individual regions and to calculate the mean velocity vector for each region, see, e.g., fig. 2.3.

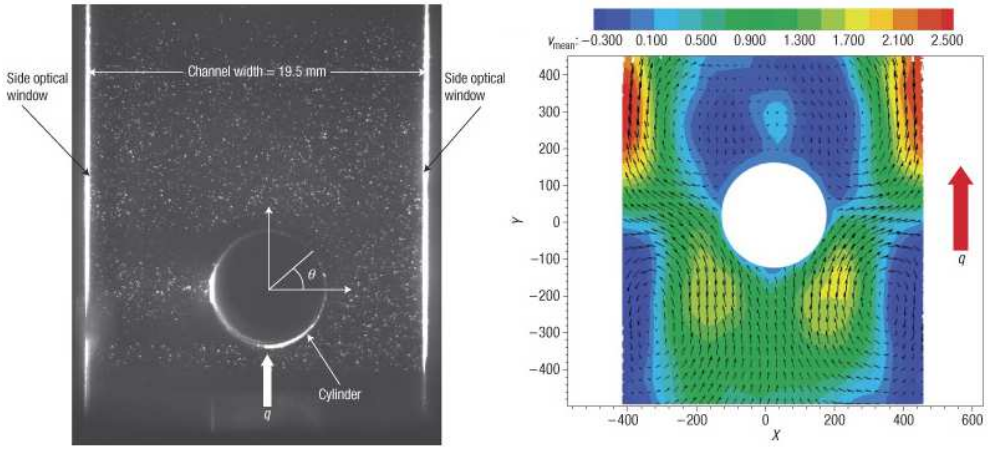

Figure 2.3: PIV study of large-scale flow around a cylinder in thermal counterflow of He II. Left: snapshot of the field of view. Seeding particles subject for visualization are polymer microspheres of 1.7 µm diameter and density 1 100 kg/m^3. Right: PIV velocity field of the same region. Source of image [40], reprinted by permission from Macmillan Publishers Ltd.

Laser Doppler velocimetry

Laser Doppler velocimetry (LDV) aims to measure the velocity of a single particle, located at a specific point within the experimental volume. This point is illuminated by two laser beams that interfere with each other. The beam interference is, however, disrupted in the presence of the particle, and the resulting

signal is Doppler-shifted due to the nonzero velocity of the particle. Combination of multiple lasers allows to obtain tridimensional velocity of the particle.

Since the velocity measurement is localized in a given point in the experimental volume, LDV is mostly suitable to probe steady flows [16]. Under such condition, one can move gradually the region of interest to obtain velocity maps, similar to those obtained by PIV, but with greater precision and underlying velocity statistics. LDV was used to study, for example, jet flow in He II counterflow seeded with H_2/D_2 particles, see [41].

Particle tracking velocimetry

In contrast with the methods described above, the particle tracking velocimetry technique (PTV) allows us to track individual particles as they move in the field of view, i.e., it does not provide any data linked to a specific location. Therefore, PTV represents a technique suitable for Lagrangian studies, while PIV and LDV are Eulerian methods. In classical turbulence, PTV is a frequently used method of great spatial and time resolution for a variety of turbulent flows [42].

3 Experimental Setup

The experiments we present in this work were performed at the Department of Low Temperature Physics. We describe here the flow visualization experimental setup. It consists of a custom-made cryostat that enables optical access to the liquid helium bath. The data acquisition system includes a laser source, relevant optical components and a fast camera. We will also present the setup for particle generation to seed the flow of liquid helium with small solid particles. Finally, we will focus on relevant data processing techniques.

3.1 Cryogenic flow visualization setup

Cryostat

We show a schematic view of the cryostat in fig. 3.1. The inner volume of the cryostat consists of two vessels, for liquid nitrogen and helium, respectively. The separation volume is evacuated. More specifically, the pressure between the two volumes is lower than 10^{-5} torr, in order to insulate cryogenic liquids from outside heat inputs.

The main purpose of the liquid nitrogen bath (kept ca. at 77 K) is to precool the helium vessel from room temperature (ca. 300 K) to ca. 100 K before the transfer of liquid helium. The middle wall of the cryostat is thermally anchored to the liquid nitrogen bath (see fig. 3.1) and protects the helium vessel from radiative heat leaks. According to the Stefan-Boltzmann law, the radiative power scales with the temperature as T^4, which means that the coating kept at 77 K decreases the heat input by a factor of $(300\,\mathrm{K}/77\,\mathrm{K})^4 \simeq 230$.

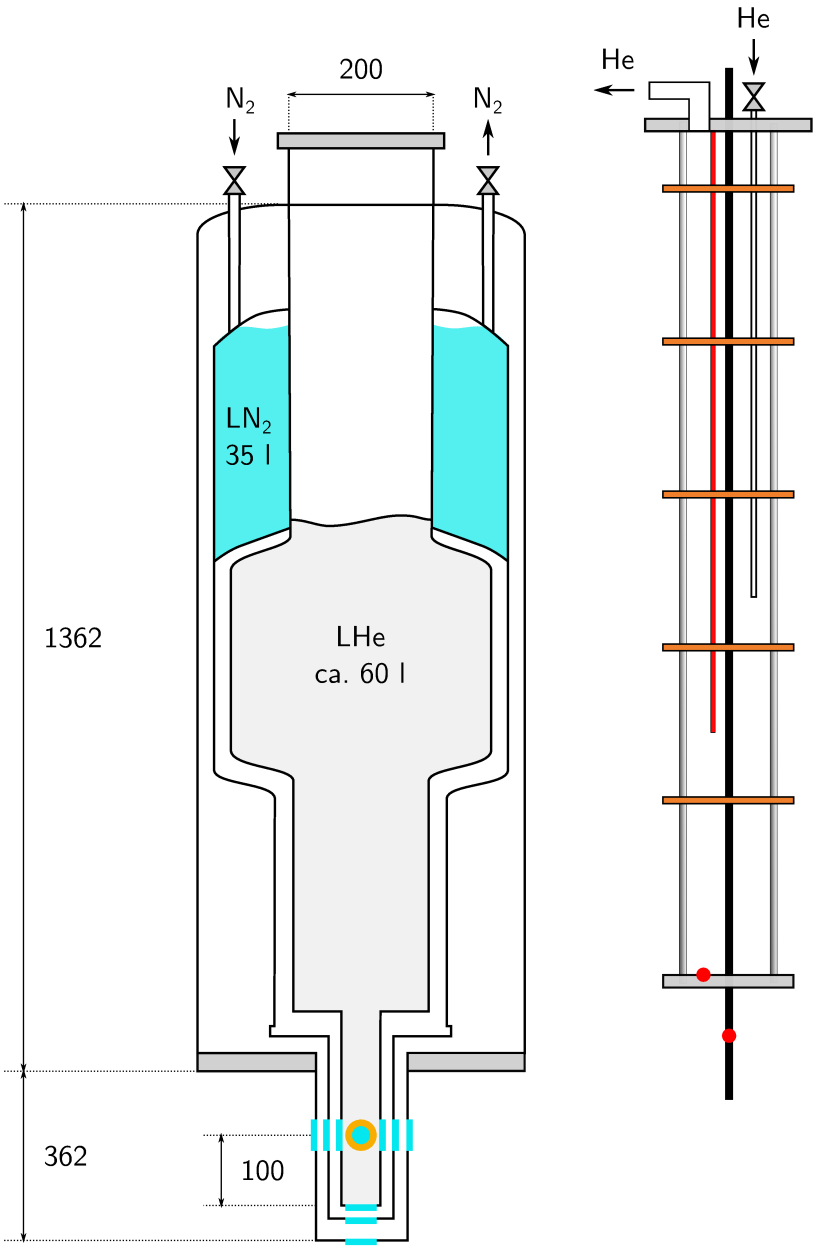

Figure 3.1: Left: simplified scheme of the cryostat. Vacuum (ca. 10^{-5} torr) is maintained between the walls for thermal insulation. The vessel for liquid nitrogen is at 77 K and is thermally anchored to the middle wall. The inner vessel for liquid helium reaches temperatures lower than 4 K. The custom-made bottom tail of the cryostat contains the experimental channel, accessible by five optical ports (four from the sides and one from the bottom). The given dimensions are in millimeters. Right: scheme of the insert. For the sake of simplicity, wiring and various ports mounted on the top flange are omitted. The red dots denote the position of two resistive thermometers, the red line indicates the level meter. Note that the meter does not exted to the bottom of the liquid helium vessel.

The vessel for liquid helium usually contains ca. 60 l of liquid at the beginning of each experiment. It is accessible from the top of the cryostat and enclosed by the top flange of the insert, see fig. 3.1 for further details. The flange is mounted with ports for wiring, the cryogenic level meter, the pressure gauge, the line for particle injection, and the line for helium transfer; two wide ports are used to pump helium vapors and to vent the cryostat, respectively.

During experiments, the helium bath is being constantly pumped by the pumping system that consists of a rotary pump and a Roots pump connected in series. The pumping rate is controlled remotely via a butterfly valve in order to maintain a constant pressure above the level of helium. In equilibrium, the vapors are saturated, i.e., their pressure uniquely corresponds to the temperature of the liquid, see fig. 3.2. As a result, by setting a constant pressure of the vapor one eventually controls the temperature of the liquid. In addition, two resistive thermometers are used to probe the temperature close to the experimental channel during the precooling phase.

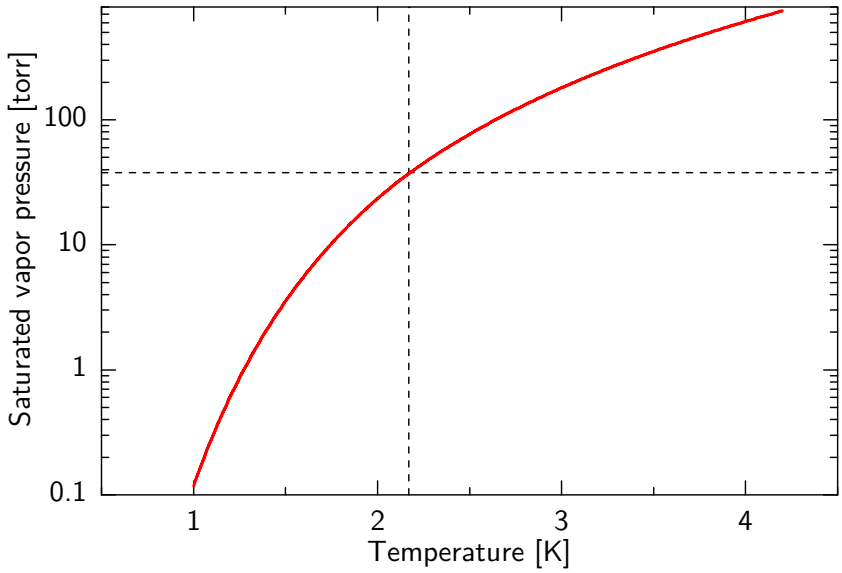

Figure 3.2: Pressure of the saturated vapor of liquid helium as a function of temperature. Data obtained from the HEPAK package [13]. The dashed lines indicate the temperature and the pressure of the superfluid transition, i.e., 2.172 K and 37.8 torr, respectively [4].

Typically, we transfer liquid helium from a transport Dewar at a pressure of ca. 760 torr, which corresponds to the temperature of 4.2 K. After the transfer, the pumping system is switched on to slowly decrease the pressure. The superfluid transition occurs at 37.8 torr [4]. The lowest pressure that the current setup is

able to maintain is ca. 0.8 torr, which corresponds to the temperature of 1.25 K, i.e., the lowest temperature we can achieve.

Experimental channel and visualization optics

At the bottom of the cryostat, the custom-made experimental channel extends from the inner vessel, see figures 3.1 and 3.3. The inner dimensions of the square channel are 50 mm (side) and 300 mm (height). The channel is mounted with five circular windows, having inner diameter of 25 mm. Four windows are located on the sides and the fifth window is mounted at the bottom.

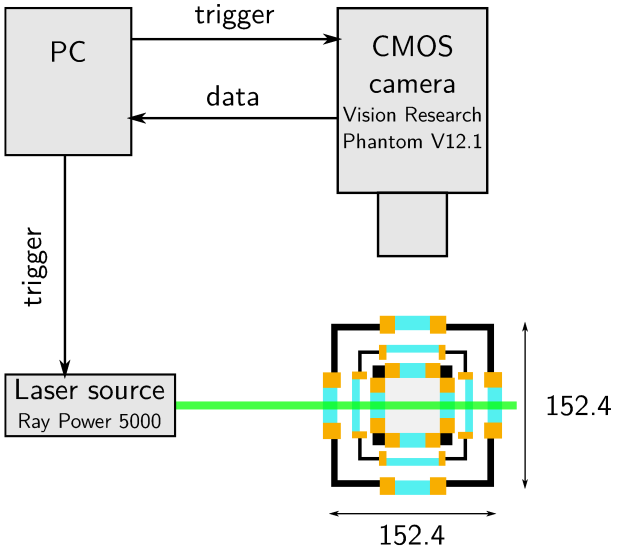

Figure 3.3: Scheme of the cryostat tail (top view). The experimental channel containing liquid helium (light gray) is of square cross section of 50 mm sides and 300 mm high. Windows are depicted in light blue and their bearings are brown. A laser sheet (ca. 1 mm thick and 20 mm high, at most) is used to illuminate the plane in the channel, to which the camera sensor is sharply focused via a macro lens. The dimensions are given in millimeters.

A long metallic shaft, located in the middle of the cryostat insert leads from the outside of the cryostat towards the experimental channel. We use the shaft to mount our experimental cells or various flow generators, as it can be moved in the vertical direction, either manually, to fine tune the position of the cell, or by a motor, to set the flow generator, such as a grid, in oscillatory motion.

The channel is illuminated by a sheet of green laser. The source of it is a solid-state laser of a few hundred milliwatts in power. The laser ray is expanded to a two-dimensional sheet by a cylindrical lens and passes through the experimental

channel. The thickness of the sheet is ca. 1 mm and its height can be set up to ca. 20 mm. Perpendicularly to the sheet, a high-speed CMOS camera is sharply focused by a macro lens on the illuminated plane to capture the light scattered by the seeding particles, see fig. 3.3. The resolution of the camera is 1280×800 pix, at the maximum frame rate of 6 kHz. The synchronization between the laser pulses and the camera shutter is controlled by a computer. The images provided by the camera are saved in series of gray scale bitmaps.

Production of solid particles

The particles we use are made of solid hydrogen or deuterium that are dispersed in the experimental channel. The process of their production is detailed in [37]. Firstly, we dilute hydrogen or deuterium gas with helium, approximately in 1 : 100 ratio. The mixture is kept at room temperature and at an overpressure of ca. 2 bar, relative to the pressure inside the cryostat. Then the gas is introduced into the liquid helium bath in series of short injections, e.g., 5 pulses of 100 ms width, each. The width and the number of pulses is controlled remotely by a PC via a solenoid valve. The quick cooldown of the mixture leads to the creation of particles whose diameter ranges from 1 µm to ca. 10 µm. We also observe that smaller and more uniformly sized particles are obtained when the mixture is injected in He I instead of He II. See fig. 3.4 for typical size distributions of the particles.

The density of solid hydrogen is 88 kg/m^3 and that of deuterium is 202 kg/m^3 [43]. Both densities do not match with that of liquid helium (145 kg/m^3, in the superfluid phase [4]). In other words, the particles are not neutrally buoyant and settle; the particles made of hydrogen tend to float on the surface of the liquid, while the deuterium ones settle on the bottom of the experimental cell. During the experiment, one can resuspend the particles by injecting pure helium gas into the experimental channel.

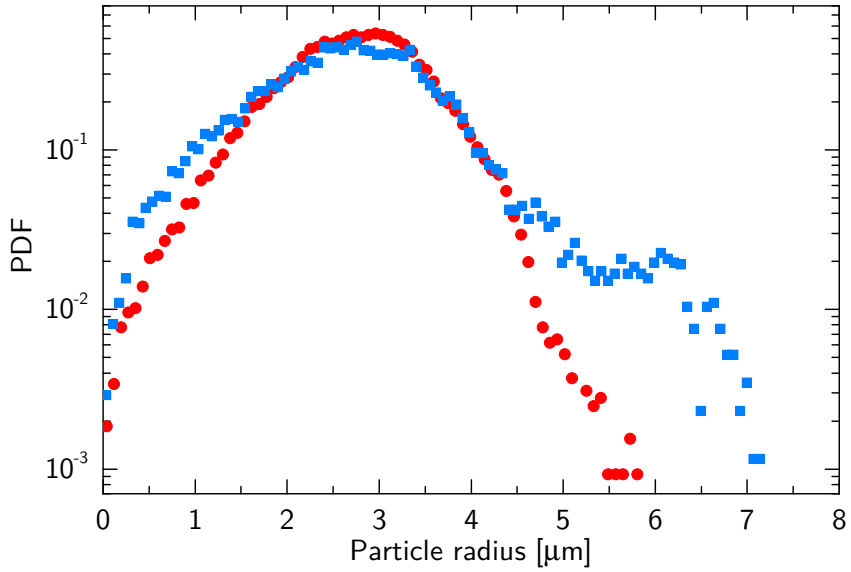

Figure 3.4: Typical size distribution of solid hydrogen (red) and deuterium (blue) particles. The size of the particles was calculated from eq. (2.1), the final settling velocity $\mathbf{u}_\infty$ was measured in quiescent He II, at ca. 1.95 K, for both types of particles. 4.1×10^4 and 2.4×10^4 velocity points are included, for hydrogen and deuterium particles, respectively.

3.2 Design of the performed experiments

As we have already stated several times, flows of He II can be obtained either mechanically or thermally. Here we present the design of two different oscillating bodies that were used to probe mechanically driven flows and the cell for the investigation of thermal counterflow.

Oscillating obstacles

We mount the oscillators at the end of the vertical metallic shaft, whose top end is connected to a step motor. The connection via a short crank provides quasi-harmonic oscillatory motion of the shaft. The amplitude of oscillations is set to 5 mm or 10 mm, while the remotely controlled frequency ranges between 0.05 and 3.0 Hz.

The first oscillating object is a cylinder of rectangular cross section. It is made of transparent Plexiglas, to reduce the absorption of the incident laser light. The cylinder is firmly attached to the bottom end of the shaft via a brass rod.

We visualize the flow shed by the cylinder in a sharply focused plane located approximately in the middle of the cylinder length, see fig. 3.5, in the rectangular field of view of $34 \times 21\,\mathrm{mm}^2$ cross section. See ref. [22] for a picture of the cylinder.

The edges of the cylinder are visible in the acquired images due to the light that is dispersed on these edges. Therefore, we post-process the raw data in order to dynamically mask these reflections by a black rectangle. Firstly, we have to find the phase and the frequency of the cylinder oscillations for each frame series. Then we can apply a dynamic mask that can gradually cover the spurious reflections in each frame, see again fig. 3.5.

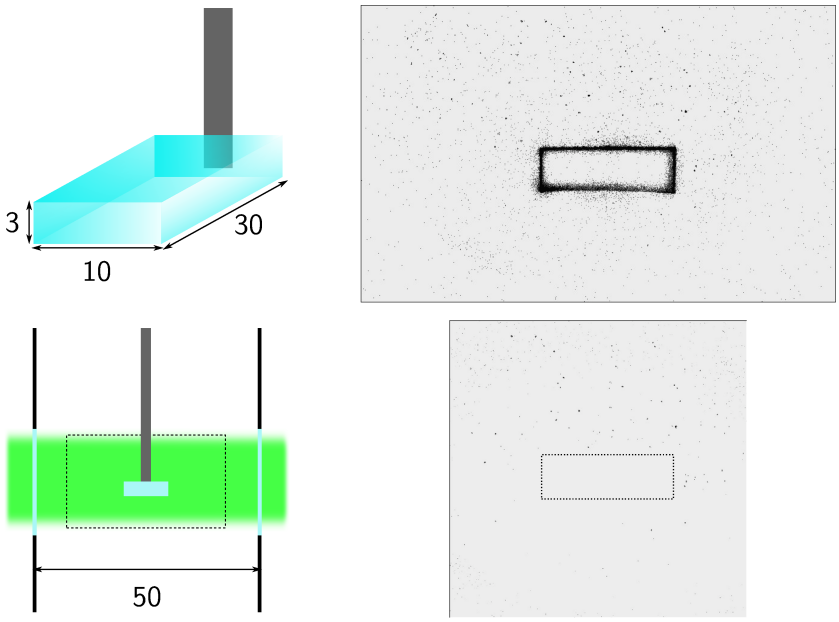

Figure 3.5: Top left: scheme of the cylinder (dimensions in millimeters). Bottom left: the position of the cylinder in the experimental channel. The laser sheet (green) illuminates the field of view of $34 \times 21\,\mathrm{mm}^2$ (dashed rectangle). Right: example of image post processing. The raw image is at the top, the image after cropping and removing the cylinder is at the bottom. The original position of the cylinder is marked by a black rectangle. Colors are inverted in both images.

The other flow generator is made of a pair of grids, see fig. 3.6. Each grid consists of 7×7 circular holes having 4 mm diameter. The holes are equidistantly distributed in a square brass block of 35 mm side. We can therefore define the relevant mesh size as $(35/7)\,\mathrm{mm} = 5\,\mathrm{mm}$. Note that the holes in the corners are occupied by a brass frame that connects the grids to the cryostat shaft. To align the grids in the center of the experimental channel, we use custom-made cardboard rings. The camera field of view, of rectangular $13 \times 8\,\mathrm{mm}^2$ cross-section, is located approximately in the middle between the grids, i.e., six times the mesh

size away from them. The remotely controlled step motor provides oscillations of 10 mm amplitude and $0.5 - 3.0$ Hz frequency.

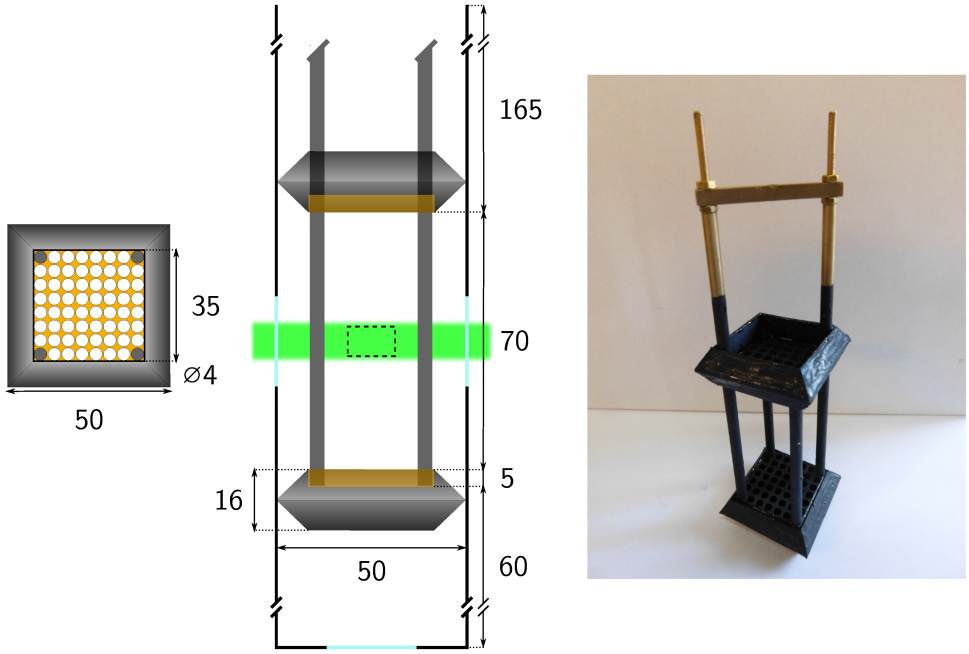

Figure 3.6: Left: top view of the grid. The cardboard ring (grey) centers the grid in the middle of the experimental channel. Middle: relative position of the grid pair in the experimental channel. The grids are shown in brown, the frame that supports the grids is in grey. The green rectangle denotes the laser sheet and the dashed rectangle indicates the field of view of 12 mm width and 8 mm height. All dimensions are in millimeters. Right: picture of the grid.

Thermal counterflow cell

The cell for thermally driven flows is depicted in fig. 3.7. It has a square cross-section of 25 mm sides and 100 mm height. A planar heater is mounted on the bottom base of the cell. It consists of a resistive meandering wire having a resistance of ca. 72 Ω, measured in He II. The power dissipated by the heater is constantly measured as the product of the relevant current and voltage. The supporting structure of the cell, including its bases, is made of brass. Instead, the walls are removable and made of glass in order to allow optical access to the cell. The capillary that allows particle injections enters the cell through the top base. Optionally, it is possible to attach a glass wall to the top base of the cell to create an observable boundary. The thickness of the glass is ca. 2 mm and its height is 80 mm.

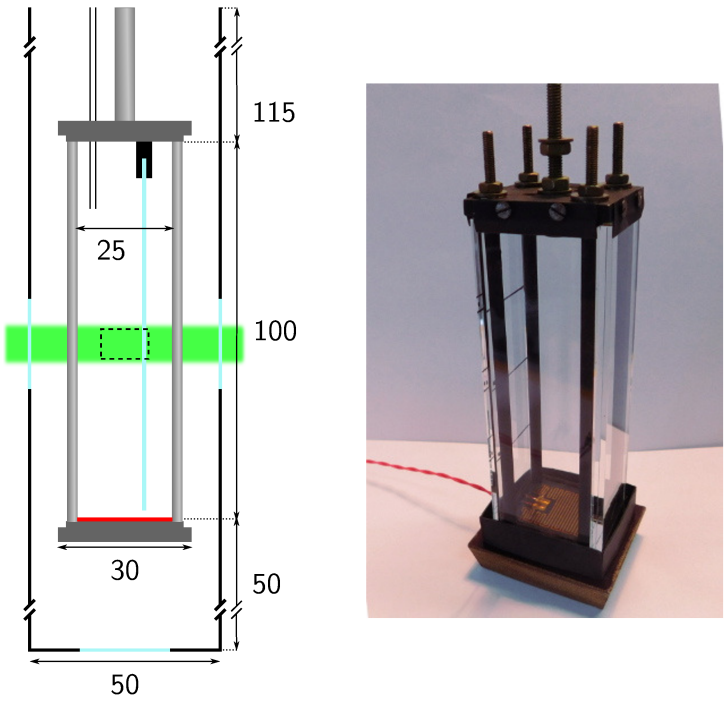

Figure 3.7: Left: scheme of the counterflow cell and of its position in the experimental channel. The red rectangle at the bottom base of the cell indicates the planar heater. When the heat is dissipated here, the counterflow is developed in the cell. It can be studied in the bulk or in the proximity of a boundary, that is, in this case, a glass wall (light blue). Particles are injected into the cell through a capillary that enters the cell in its top base. The visualized field of view of $13 \times 8\,\mathrm{mm}^2$ is depicted as a black dashed rectangle; it is slightly smaller in the case of the presence of the boundary. All dimensions are in millimeters. Right: picture of the cell without the inner wall.

3.3 Image processing

The data acquired by the camera are stored as series of 1 Mpix bitmap images. Each image contains from 10 to 100 particles that appear as small bright points. The main goal of the relevant image processing is to detect these particles and measure their position within the image. The second goal consists of linking individual particle positions into trajectories across consecutive frames.

We carry out this procedure by using the open source particle tracking software Mosaic Suite [44] embedded in the image processing software ImageJ. Firstly, the code looks for the local maxima of brightness in the frames to identify individual particles. Their positions are calculated with sub-pixel resolution from a two-dimensional Gaussian fit. After that, another algorithm is employed to connect the particles into trajectories. The algorithm estimates particle positions

in the following frame based on their positions in previous ones. If the estimated position matches with the position of a detected particle within certain error, the trajectory is extended. The algorithm is also capable of such linking across multiple frames. Note, however, that the trajectories are of different lengths, due to the fact that we track only a two-dimensional plane in the flow having three dimensions. In other words, the particles are likely to leave the illuminated plane and disappear from the image sequence.

The obtained numerical data are further processed in order to improve the quality of the dataset. Firstly, we filter out the trajectories containing less than 5 particle positions. Then we smoothen the remaining trajectories by using the linear smoothing algorithm. Finally, we interpolate missing particle positions. These missing positions are due to the fact that the same particle is not detected in every consecutive frame, but yet the original trajectory is recovered.

4 Results and Discussion

The flows of He II that are generated mechanically and thermally are fundamentally different. In the case of thermal counterflow, the normal and superfluid components move, on average, in opposite directions. Such a flow has no obvious classical analogue. For mechanically driven flows instead, the two components of He II are locked together via the mutual friction force. As a result, large scale mechanically driven flows of He II should not differ from viscous ones [45]. More precisely, it is expected that He II behaves as a single fluid with a finite effective viscosity.

For example, the flow due to an oscillating cylinder displays macroscopic (large-scale) eddies of a few millimeter size that look similar in He I and in He II [22]. The strength of the vortices can be quantified from the available particle positions and velocities, as a coarse-grained vorticity estimate. Despite the same appearance, we observed that the strength of the vortices differs in normal liquid and superfluid ^{4}He, when the scale we resolve becomes smaller than the estimated intervortex distance.

These results strongly indicate that the features characteristic for quantum turbulence are more pronounced at small enough length scales. In the following we define the smallest probed scale ℓ_{exp} and the characteristic scale of quantum flows, i.e., the quantum scale ℓ_{q}. The use of solid particles of finite size and their tracking with a finite time resolution limits the smallest accessible ℓ_{exp}. There are two relevant limiting factors. Firstly, we can only probe scales larger than the size (diameter) d of the particles. In our case, d ranges between ca. 1 µm and 14 µm, see fig. 3.4. The second factor is due to the finite temporal resolution of the camera and, usually, exceeds the former. A relevant length scale can be hence defined as the mean displacement δ of the particles between the consecutive frames. We can obtain δ directly from the experimental data or we can calculate it as the ratio between the typical velocity and the camera frame rate.

Subsequently, the smallest accessible scale is

$$\ell_{\mathrm{exp}} = \max\{d, \delta\}. \tag{4.1}$$

Note that $d < \delta$ for the experiments presented below, in the range of investigated parameters, i.e., the smallest ℓ_{exp} is limited by the camera frame rate. If this is indeed the case, we can also artificially increase ℓ_{exp} by removing particle positions from the measured trajectories. Estimates of the quantum length scale ℓ_{q} are dependent of the type of the flow and will be discussed below.

4.1 Universality of particle motions at small scales

Here we present results obtained in thermal counterflow (in the bulk and in the proximity of a wall) and in mechanically driven flows due to an oscillating cylinder. We use the measured particle positions to calculate their velocities in the horizontal and vertical directions. For a trajectory containing N positions we obtain N velocity points as

$$\begin{aligned} \mathbf{u}_1 &= \frac{\mathbf{r}_2 - \mathbf{r}_1}{\tau}, \\ \mathbf{u}_i &= \frac{\mathbf{r}_{i+1} - \mathbf{r}_{i-1}}{2\tau} \quad \text{for } i \in \{2, \ldots, N-1\}, \\ \mathbf{u}_N &= \frac{\mathbf{r}_N - \mathbf{r}_{N-1}}{\tau}. \end{aligned} \tag{4.2}$$

where τ denotes the time separation between two consecutive particle positions.

We process the obtained data statistically and we plot them in the form of probability density function (PDF). The distributions are centered around their mean and normalized by their standard deviation. As a result, the distributions are of zero mean, unitary variance and unitary area, so that we can directly compare different data sets.

We plot the PDFs of the normalized horizontal velocity in figures 4.1 and 4.2, for small and large scales, respectively. We quantify the investigated scale via a parameter R defined as $R = \ell_{\mathrm{exp}}/\ell_{\mathrm{q}}$; its numeric values are specified in the figure legends. In the case of thermal counterflow, we set $\ell_{\mathrm{exp}} = u_{\mathrm{abs}}\tau$, where u_{abs} denotes the mean absolute velocity of the particles obtained at the lowest R and τ is the time separation defined above. The calculation of the relevant quantum length scale is specified in [46]. We estimate $\ell_{\mathrm{q}} \simeq 1/(\gamma|v_{\mathrm{ns}}|)$, where γ

is a parameter whose approximate value can be obtained from experiments [47] and $|v_{ns}|$ indicates the counterflow velocity.

In the case of the mechanically driven flow, we calculate ℓ_{exp} based on the motion of the submerged cylinder. We estimate that a typical flow velocity is approximately equal to the peak velocity of the cylinder, i.e., $2\pi fa$, where f and a are the frequency and amplitude of oscillations, respectively. It therefore follows that ℓ_{exp} can be expressed as $\ell_{exp} = 2\pi fa\tau$. The quantum scale can be estimated as a relevant analogue of the Kolmogorov length scale η, dependent on ν and ϵ, i.e., kinematic viscosity and energy dissipation rate, see eq. (1.14). The latter can be calculated, for homogeneous isotropic turbulence, as $\epsilon = \nu\Omega^2$, where Ω indicates the mean vorticity. In He II we can estimate the mean vorticity from a custom-defined parameter θ that can be seen as a Lagrangian analogue of the coarse-grained vorticity [22]. Ω^2 can be subsequently expressed as $\Omega^2 \simeq \langle\theta^2\rangle$, where the angle brackets indicate the ensemble average of θ^2. As a result, $\epsilon \simeq \nu\langle\theta^2\rangle$ and eq. (1.14) yields

$$\ell_q \simeq \left(\frac{\nu^2}{\langle\theta^2\rangle}\right)^{1/4}. \tag{4.3}$$

Table 4.1: Summary of the experimental data sets plotted in fig. 4.1. The first two data sets were obtained in the flow generated by an oscillating cylinder, at 0.05 Hz frequency and 5 mm amplitude; the middle and last pair of data sets correspond to wall-bounded and bulk counterflow, respectively. P: type of particles; T: temperature in K; R: ratio of the probed to quantum length scales; ℓ_q: quantum length scale in µm; $\langle u\rangle$ and $\sigma(u)$: mean value and standard deviation of the particle horizontal velocity u in mm/s; w: heat flux supplied to the He II bath in W/m^2 (relevant only for counterflow).

Symbol (figures 4.1 & 4.2)	P	T	R	ℓ_q	$\langle u\rangle$	$\sigma(u)$	w
black squares	D_2	1.24	0.07	235	-1.2	1.9	–
green open squares	D_2	1.50	0.07	226	1.0	2.4	–
blue triangles	H_2	1.95	0.03	145	0.2	1.2	293
orange open triangles	H_2	1.95	0.06	73	0.2	1.3	587
red filled circles	H_2	1.77	0.09	70	-0.3	1.6	612
black open circles	D_2	1.77	0.14	70	0.5	1.9	608

The kinematic viscosity of He I is tabulated in ref. [4]. Contrarily, the effective kinematic viscosity of He II as a function of temperature is known to date only with a limited precision [47]. We can thus estimate its value as a zero-order approximation. Since the temperature dependence of the He II kinematic viscosity is weak, we set, for the sake of simplicity, its value to be approximately constant and equal to $\nu \simeq 1.66 \times 10^{-8}\,\mathrm{m^2/s}$, i.e., the value of the kinematic viscosity of He I at a temperature close to the superfluid transition [22].

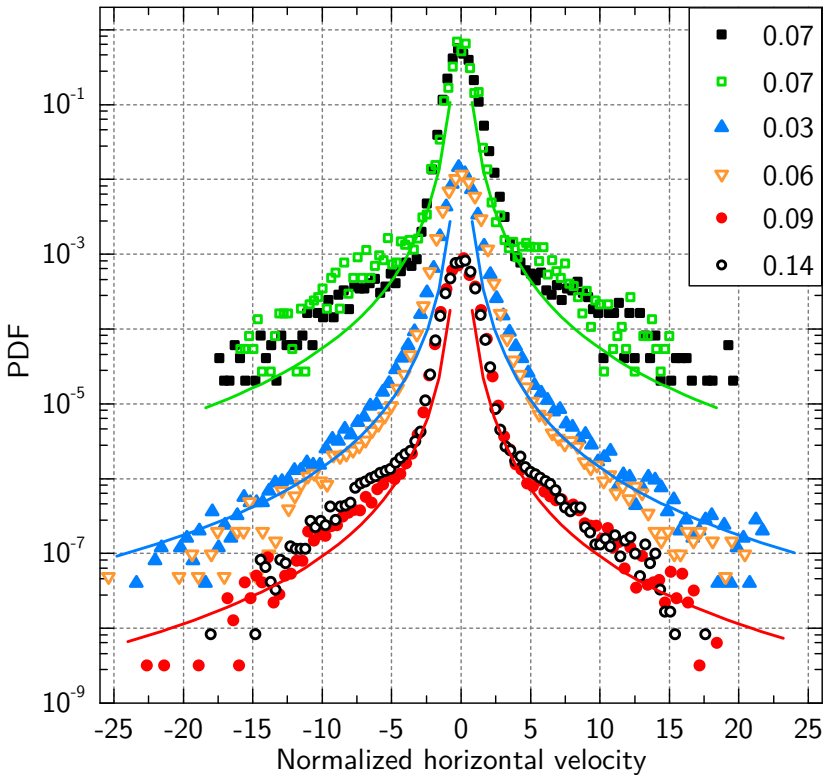

Figure 4.1: Probability density function (PDF) of the normalized horizontal velocity of six data sets. Pairs of data sets are vertically shifted for the sake of clarity. Empty green and black squares: mechanically driven flows due to an oscillating cylinder; empty orange and blue triangles: counterflow in the proximity of a wall; empty black and red circles: counterflow in the bulk. See table 4.1 for more details. Values in the legend indicate the relevant values of R. Green, blue and red solid lines indicate the same $|u_{\mathrm{norm}}|^{-3}$ scaling.

Figure 4.1 shows the velocity distributions of six data sets, including mechanically driven flows, bulk and wall-bounded counterflow of He II, see tab. 4.1 for details. For all the data sets $R = \ell_{\mathrm{exp}}/\ell_{\mathrm{q}} < 1$, see the legend of the same figure. This means that the distributions reflect the small scale nature of He II and, consequently, reveal several non-trivial features.

The shape of the distributions is almost identical for mechanically driven flows (green and black squares), counterflow close to the wall (blue and orange triangles) and bulk counterflow (red and black circles), despite the difference between mechanically and thermally generated flows at large scales.

This is the most striking outcome and we call it the small-scale universality of quantum turbulence. It seems that the underlying dynamics of the particles, at small scales, does not depend on the large-scale flow. Instead, the shape of the distribution curve is governed mainly by the parameter R.

Note that only some distributions we measured are plotted here. Other results were obtained at different cylinder frequencies and amplitudes, as well as at different values of the heater power, and at temperatures ranging from 1.2 K to 2.2 K. We observe that these results overlap with the shown data too. This indicates that the behavior just outlined is insensitive of temperature and the relevant flow forcing, which reinforces the idea of universality just outlined.

Small, but visible differences can be seen in the shape of distributions obtained in the bulk and the wall-bounded counterflow. More specifically, the distribution tails appear to be wider in the bulk; see also fig. 4.3 below for relevant flatness values.

Our second observation is that the distribution shape does not match with similar experimental results obtained in viscous fluids, see, e.g., ref. [48]. Velocity distributions, normalized in the same manner as in here, and obtained, e.g., in water, have shapes similar to that of the standard Gaussian distribution. Instead, the distributions we measure in He II are characterized by wide non-Gaussian tails. This outcome is in agreement with recent experimental results [46, 49] in other counterflow experiments. More precisely, the central parts of the distributions, up to ca. 2-times the standard deviation, are broadened probably due to the finite precision of the tracking algorithm. Non-Gaussian tails span from ca. 5-times up to 25-times the standard deviation and follow the power-law scaling with -3 exponent (see the solid lines in fig. 4.1), again in agreement with the references cited above.

A simple model can be introduced to interpret the power-law scaling [46]. Let us consider the radial velocity profile of the superfluid component v_s generated by a single straight vortex, specified by eq. (1.11). The probability density function PDF(v_s) that describes the distribution of different values of v_s in a 2D plane

perpendicular to the vortex line is

$$\mathrm{PDF}(v_\mathrm{s}) = \frac{\mathrm{d}P}{\mathrm{d}v_\mathrm{s}} \sim \frac{2\pi r \mathrm{d}r}{\mathrm{d}v_\mathrm{s}}, \tag{4.4}$$

where $\mathrm{d}P$ represents the probability of measuring a velocity inside the interval $(v_\mathrm{s}; v_\mathrm{s} + \mathrm{d}v_\mathrm{s})$. Within the considered 2D plane, this interval is represented by an annulus of radius r and thickness $\mathrm{d}r$. From eq. (1.11) one can express r as a function of v_s ($r \sim 1/v_\mathrm{s}$) and calculate $\mathrm{d}r/\mathrm{d}v_\mathrm{s} \sim 1/v_\mathrm{s}^2$. As a result, we obtain $\mathrm{PDF}(v_\mathrm{s}) \sim {v_\mathrm{s}}^{-3}$, which is in agreement with the scaling law of experimentally accessible particle velocities.

A more elaborate model of particle dynamics can be developed, see attachment [A1]. Besides the force that attracts a particle towards a vortex, one must consider that particles are often trapped on vortex lines. The dynamics of vortex reconnections can thus act as the source of the excessive particle velocity [49]. However, the maximum particle velocity (i.e., the maximum width of the relevant PDF) is limited due to the nonzero drag force of the normal component. More specifically, if the particle velocity is large enough, the drag force can exceed the trapping force and subsequently the particle can detrap. Moreover, a simplified model of a single vortex, outlined above, can be used to calculate the lower limit of the non-classical tail width, i.e., the velocity before particle trapping occurs. See [A1] for further details.

We conclude that our observations strongly indicate that relevant particle motions, probed at scales smaller than ℓ_q, clearly display non-classical physics. From the shape of the distributions, we can argue that the motion of seeding particles is mainly influenced by the presence of individual quantized vortices that, as we have shown in the theoretical part, can alter the motions of small enough particles.

Furthermore, the value of R can be increased artificially, by removing particle positions from the trajectories obtained experimentally. We replot the six data sets from fig. 4.1 in fig. 4.2, for $R > 1$, to compare them. Again, the distributions overlap, but now they follow the standard Gaussian distribution (denoted by a solid line), similarly to what is observed in classical flows [48].

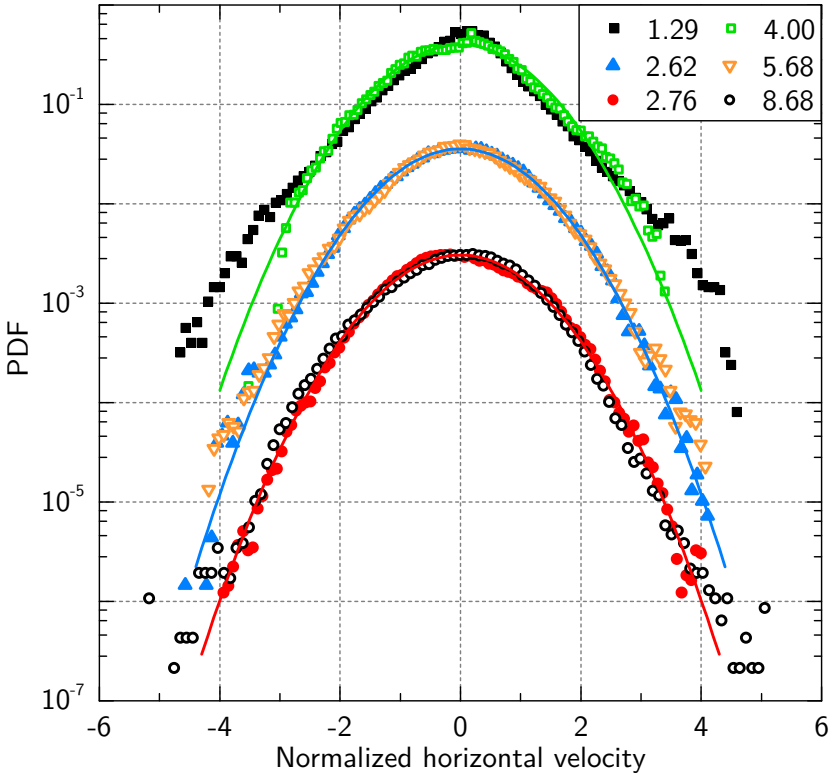

Figure 4.2: PDF of the normalized horizontal velocity of the same data sets as in fig. 4.1, at scales larger than unity. See fig. 4.1 for more detailed information. Again, the data sets are shifted vertically. Solid lines denote the standard Gaussian distribution, i.e., of zero mean and of unitary variance.

Is is evident that the physical picture of quantum flows of He II is strongly dependent on the observed length scale: apparently, wide tails of velocity distributions gradually vanish as the scale increases. We can evaluate this transition in terms of flatness, i.e., the fourth moment of the distributions. In fig. 4.3 we plot the flatness as a function of the parameter R for several data sets, including both mechanically and thermally driven flows. While wide tails at small scales, i.e., $R < 1$, result in large values of flatness, up to ca. 50, Gaussian-like distributions at large scales ($R > 1$) display values close to 3, which is the exact flatness of the standard Gaussian distribution. Note that for measurements performed in He I (cyan empty diamonds), i.e., in a viscous fluid, the value of flatness remains equal to ca. 3, independently of the probed length scale (here the typical flow scale was defined as the Kolmogorov scale η, see eq. (1.14). The flatness of velocity distributions can be therefore seen as a simple, yet powerful indicator of quantum features in He II flows.

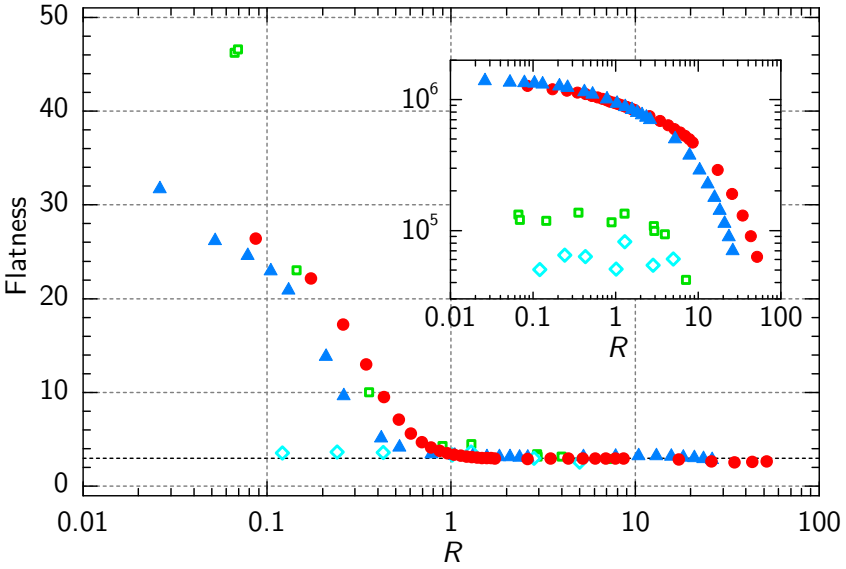

Figure 4.3: Flatness (fourth moment) of the horizontal velocity as a function of R (see text for details). The green squares are obtained in the proximity of the oscillating cylinder, in He II (between ca. 1.2 K and 1.7 K); the cyan diamonds represent the data obtained in the same experimental geometry in normal liquid He I (ca. 2.2 K). Accordingly to the previous notation, the blue triangles indicate counterflow close to a boundary and the red circles denote bulk counterflow. The black dashed horizontal line denotes the flatness of the standard Gaussian distribution. Insert: number of points as a function of R. Note that the measured trajectories are not of the same length, i.e., the decrease of statistics for counterflow is due to the artificial removal of velocity points from the trajectories. In the case of the oscillating cylinder data sets, individual data points were obtained in different experimental runs.

4.2 Large-scale grid turbulence

In the previous section we demonstrated that turbulent flows of He II display both quantum and classical features. Tracking of relatively small particles revealed that He II flows differ from classical ones at small scales. At large scales instead, He II flows seem to mimic classical (viscous) turbulence. However, detailed information on possible similarities or differences between the large-scale flows of He II and flows of viscous fluids is still lacking. Here we report on a systematic study of mechanically generated turbulence, by a pair of grids, in He II, and probed by solid deuterium particles.

The grid pair oscillates in phase, see fig. 3.6, at frequencies up to 3 Hz. In classical fluid dynamics, the use of grids as turbulence generators is well established, as they can generate nearly isotropic turbulence [50]. Nevertheless, the use of

oscillating grids in He II is scarce. Honey et al. [51] reported on several experiments regarding the propagation of turbulent fronts in He II and relevant vorticity profiles in a channel mounted with a grid. Sy et al. [52] studied instead the dispersion of small solid particles in grid-generated turbulent flows. At sub-kelvin temperatures, researachers use microscopic vibrating grids to create and probe quantum turbulence in pure superfluids [53].

The quantum scale ℓ_{q} of grid flows can be estimated by using the analogy with viscous flows. More specifically, we write a quasiclassical relation for the energy dissipation rate as $\epsilon = \nu_{\mathrm{eff}}(\kappa L)^2$, where κL is seen as the mean vorticity in quantum flows and ν_{eff} is the effective kinematic viscosity [47], whose value is of the order of $10^{-8}\,\mathrm{m}^2/\mathrm{s}$. Simultaneously, the energy dissipation rate is linked to the motion of the grids. One can express ϵ as $\epsilon = u_{\mathrm{grid}}^3/M$, where u_{grid} is the grid peak velocity and M is the grid mesh size. As a result, the quantum length scale is

$$\ell_{\mathrm{q}} = \sqrt{1/L} = \sqrt[4]{\frac{\kappa^2 \nu_{\mathrm{eff}} M}{u_{\mathrm{grid}}^3}}. \tag{4.5}$$

Furthermore, we compute the approximate probed scale ℓ_{exp} based on u_{grid} as $\ell_{\mathrm{exp}} \simeq u_{\mathrm{grid}}\tau$. As a result, the ratio $R = \ell_{\mathrm{exp}}/\ell_{\mathrm{q}}$ is a function of the grid frequency only (all the other parameters remain constant). Here we restrict ourselves only at experiments performed at 1 Hz oscillation frequency and 10 mm amplitude, which result in $R \simeq 23$.

Table 4.2: Velocities and velocity increments obtained in the flow shed by a pair of oscillating grids. We present only data sets obtained at 1 Hz grid oscillation frequency and 10 mm amplitude. The relevant length scale ratio is $R \simeq 23$. T denotes the temperature in K, $\mathrm{Re} = u_{\mathrm{grid}}M/\nu$ indicates the mesh Reynolds number (here ν represents the kinematic viscosity of the normal component). Angle brackets represent relevant mean values, σ indicates the standard deviation of the velocity (u_x, u_y, in mm/s) and velocity increment ($\mathrm{d}u_x$, $\mathrm{d}u_y$, in $\mathrm{mm/s}^2$), respectively. Positive values indicate right and upward directions, respectively.

T	Re	$\langle u_x \rangle$	$\sigma(u_x)$	$\langle u_y \rangle$	$\sigma(u_y)$	$\langle \mathrm{d}u_x \rangle$	$\sigma(\mathrm{d}u_x)$
2.53	14 200	2.2	4.2	3.2	5.2	-2.2	197
1.95	32 900	0.4	3.8	1.0	5.4	-0.6	191
1.75	35 000	0.5	4.2	-1.1	5.2	-1.1	171
1.50	32 300	-1.5	3.8	-1.7	6.3	-1.7	171
1.27	24 900	-0.6	4.7	4.6	7.8	-2.2	197

We plot the velocity distributions for five data sets in fig. 4.4; see also tab. 4.2 for additional information. We observe that the large scale velocity distributions are nearly Gaussian (black dashed line), which is in agreement with former results. Small, but visible deviations from the Gaussian shape are probably due to flow anisotropy.

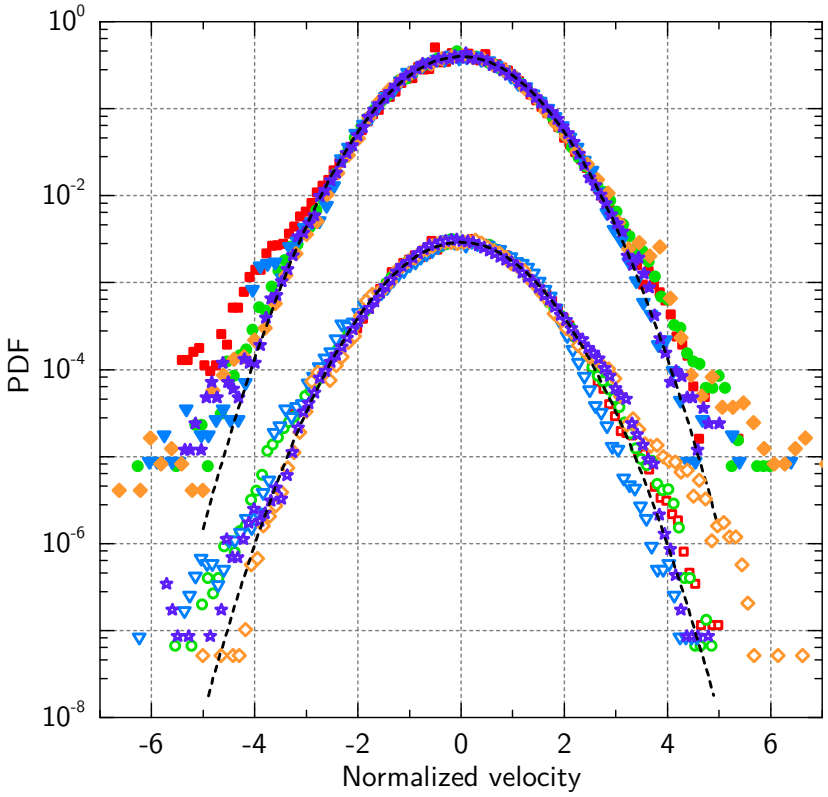

Figure 4.4: Velocity distributions in the horizontal (filled symbols) and vertical (empty symbols) directions. Note that the grid pair oscillates in the vertical direction. Both distributions are centered around their mean values and scaled by their standard deviations. All the data sets are obtained for 1 Hz oscillation frequency and 10 mm amplitude. Data series differ in temperature. Red squares: 2.53 K (He I); green circles: 1.95 K; blue triangles: 1.75 K; orange diamonds: 1.50 K; violet stars: 1.27 K. Both distributions follow the Gaussian distribution (dashed black lines). For the sake of clarity, distributions in the vertical direction are shifted downwards.

Another quantity that is accessible from the available particle positions is the (horizontal and vertical) velocity increment, defined as

$$\mathrm{d}\mathbf{u}_i = \frac{\mathbf{u}_{i+1} - \mathbf{u}_{i-1}}{2\tau} \quad \text{for } i \in \{2, \ldots, N-1\}, \tag{4.6}$$

i.e., from N velocity points one obtains $N-2$ velocity increments. This quantity does not represent particle accelerations; for a faithful calculation of the accel-

eration from Lagrangian tracks, one needs to oversample them, i.e., the data sampling rate should be a few times larger than the desired time resolution [54]. More likely, the velocity increments can be seen as a measure of velocity variations due to particle accelerations or decelerations.

We plot the horizontal velocity increments in fig. 4.5, for the same data sets as in the previous figure. The distributions are again centered around their mean values and normalized by their standard deviations. We observe that their shape is strongly non-Gaussian, having tails spanning up to ca. 25-times the standard deviation. This observation is consistent with similar measurements in water by Mordant et al., at scales smaller than the integral scale, but larger than the Kolmogorov scale [55].

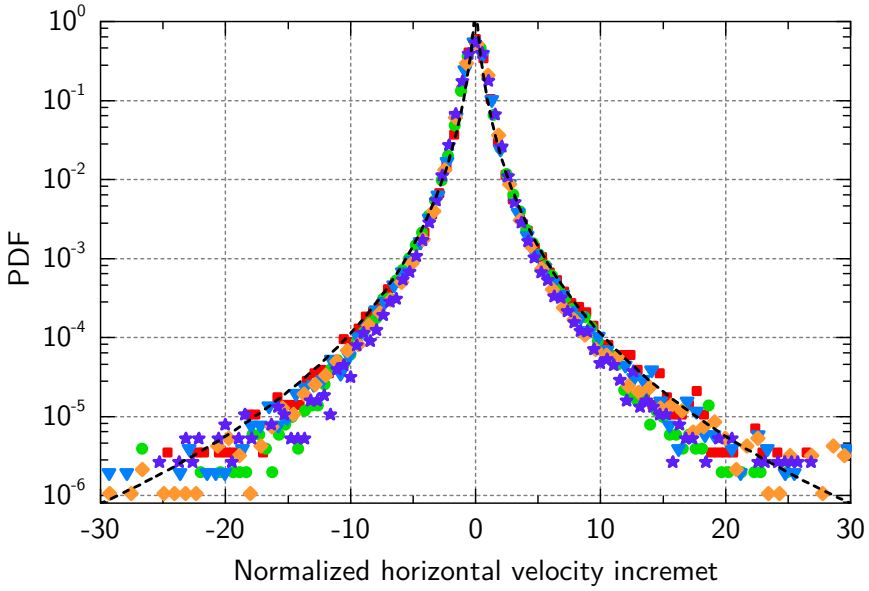

Figure 4.5: PDFs of horizontal velocity increments, centered and normalized. We plot the same data sets as in fig. 4.4: red squares: 2.53 K; green circles: 1.95 K; blue triangles: 1.75 K; orange diamonds: 1.50 K; violet stars: 1.27 K. The black dashed line represents eq. (4.7), i.e., the theoretical fit for viscous flows [56].

Mordant et al. [56] found that the distribution for ideal tracers in classical turbulence is of the form

$$\mathrm{PDF}(\mathrm{d}u_{\mathrm{norm}}) = \frac{\exp(3s^2/2)}{4\sqrt{3}} \left[1 - \mathrm{erf}\left(\frac{\ln|\mathrm{d}u_{\mathrm{norm}}/\sqrt{3}| + 2s^2}{\sqrt{2}s}\right)\right], \tag{4.7}$$

where $s = 1$ and $\mathrm{d}u_{\mathrm{norm}}$ indicates the normalized velocity increment. This function is plotted in fig. 4.5 as a black dashed line and fits also our data. More precisely, the measured data points are slightly below the theoretical curve. This

is probably due to particle inertia (keep in mind that the seeding particles are made of deuterium, which is slightly heavier than liquid helium). Nonetheless, a good agreement with the theoretical curve strongly suggests that in the range of investigated parameters, there is no difference between classical and large-scale quantum flows. These findings are complementary to similar results obtained in thermal counterflow [57].

Summary

We can summarize our findings as follows. Hydrodynamics of He II, probed at scales smaller than the mean intervortex distance ($R < 1$), differs from that of viscous fluids. We argued that the seeding particles, subject of our experimental investigations, are influenced, at small scales, mainly by quantized vortices that attract and trap these particles. The robustness of this observation is emphasized by the fact that the same behavior is observed in both mechanically and thermally driven flows, in contrast with the fact that their large scale flow structures are fundamentally different. Moreover, we see no obvious dependence on temperature or flow forcing (i.e., the cylinder oscillation frequency or the heater power).

Small differences between the bulk and wall-bounded counterlow distributions suggest that the vortex line density close to solid boundaries is slightly larger, i.e., the computed values of the R parameter may be underestimated. This is also supported by the horizontal shift between the respective counterflow data in fig. 4.3.

Contrarily, at large scales, the apparent particle dynamics is similar to that of viscous flows. We observed that the influence of quantized vortices gradually vanishes with the increasing scale, up to scales larger than the mean intervortex distance ($R > 1$). Once these scales are reached, velocity and velocity increment distributions, measured in mechanically or thermally driven flows of He II, overlap the same results obtained in viscous fluids. Consequently, these results reinforce the idea that quantum turbulence does not differ from the classical one, at least in the scope of low-order statistics of particle dynamics.

5 Conclusions

The hydrodynamics of superfluid flows of He II is very rich. It includes the flow of the viscous normal component, that of the inviscid superfluid component, and their dynamic interactions with the tangle of quantized vortices. We investigated flows of He II that were generated either mechanically or thermally, at temperatures spanning between 1.2 K and 2.5 K. We observed the motions of relatively small particles of solid hydrogen and deuterium, suspended in the fluid, and tracked their positions in time. The extracted particle positions were used for the computation of their velocities and velocity increments.

We observed that the shapes of the normalized velocity distribution, obtained in different experiments (flow due to an oscillating cylinder and channel counterflow, in the bulk and close to a boundary), at scales smaller than the mean intervortex spacing, do not depend on the imposed large-scale flow. Moreover, the distributions obtained at different temperatures and different intensities of the relevant flow forcing overlap. This likely indicates that the small-scale particle dynamics in He II is universal and dependent only of the probed length scale. We also showed that the observed dynamics is non-classical and can be linked with the interactions between particles and quantized vortices. We published these results in Physical Review B, see attachment [A1].

Note, however, that the respective flows of He II were not investigated to the fullest extent. We proposed a simple model of one straight quantized vortex that attracts one particle (see eq. 4.4) to explain the observed velocity distributions at small scales. In reality, the vortices are not straight and dynamically reconnect with other vortices. These effects release energy in the form of Kelvin waves, that can be directly observed by decorating the vortices with trapped solid particles [24]. The presence of these waves is likely to influence the observed particle motions, but an experimental study is yet to be performed.

Secondly, we performed a detailed study on the large-scale flows of He II that were generated mechanically, by a pair of oscillating grids. Large statistical data sets, obtained at different temperatures, were used to calculate velocity and velocity increment distributions. We observed that the shape of both distributions is independent of temperature and, more importantly, the distributions are in general agreement with similar results obtained in classical flows. More specifically, we observed that the velocity distributions are quasi-Gaussian and velocity increment distributions follow eq. (4.7). The obtained results support the idea that large-scale flows of He II, generated mechanically, faithfully mimic turbulent flows of viscous fluids, as the force of mutual friction locks the two components of He II into a single (large scale) velocity field. These results were presented at scientific conferences [A2-A4] and submitted for publication in the Journal of Fluid Mechanics.

The comparison between large-scale flows of He II and those of viscous fluids can be further extended. One possibility for future studies lies in the investigation of energy dissipation in turbulent flows and in the resulting time irreversibility based on the observation of longitudinal velocity increments [58]. Another interesting feature that is connected with large scales of turbulence is the dispersion of seeding particles [59]. Although the first measurements of the so-called preferential concentration of particles have been already carried out [52], an extenstive comparative study is lacking.

In conclusion, the presented study extends the current knowledge on turbulence in cryogenic helium at small scales, and clarifies what are the similarities and differences between quantum and classical turbulence at a large variety of length scales. The study of quantum turbulence, alongside with possible analogies between superfluid ^{4}He and viscous fluids, may contribute to the general understanding of viscous fluid turbulence, confirming its role as a vivid branch of fluid dynamics and low-temperature physics.

Bibliography

[1] H. Kamerlingh Onnes. The liquefaction of helium. *KNAW Proceedings*, 11:168–185, 1909.

[2] D. Van Delft and P. Kes. The discovery of superconductivity. *Physics Today*, 63:38–43, 2010.

[3] L. Skrbek. *Fyzika nízkých teplot*, volume 1. Matfyzpress, Prague, 2011.

[4] R. J. Donnelly and C. F. Barenghi. The observed properties of liquid helium at the saturated vapor pressure. *Journal of Physical and Chemical Reference Data*, 27:1217–1274, 1998.

[5] P. Kapitza. Viscosity of liquid helium below the λ-point. *Nature*, 141:74, 1938.

[6] E. L. Andronikashvili. A direct observation of two kinds of motion in helium II. *Journal of Physics – USSR*, 10:201, 1946.

[7] J. F. Allen and J. Reekie. Momentum transfer and heat flow in liquid helium II. *Mathematical Proceedings of the Cambridge Philosophical Society*, 35:114–122, 1939.

[8] L. Tisza. Transport phenomena in helium II. *Nature*, 141:913, 1938.

[9] L. D. Landau. Theory of the superfluidity of helium II. *Physical Review*, 60:356, 1941.

[10] R. P. Feynman. Application of quantum mechanics to liquid helium. *Progress in Low Temperature Physics*, 1:17–53, 1955.

[11] C. F. Barenghi, L. Skrbek, and K. R. Sreenivasan. Introduction to quantum turbulence. *Proceedings of the National Academy of Sciences*, 111(Suppl. 1):4647–4652, 2014.

[12] C. Enss and S. Hunklinger. *Low-Temperature Physics*. Springer-Verlag, Berlin, Heidelberg, 2005.

[13] V. D. Arp and R.D. McCarty. Thermophysical properties of helium-4 from 0.8 to 1500 K with pressures to 2000 MPa. *NIST Technical Note 1334*, 1989.

[14] L. Onsager. Statistical hydrodynamics. *Il Nuovo Cimento*, 6:279–287, 1949.

[15] W. F. Vinen. The detection of single quanta of circulation in liquid helium II. *Proceedings of the Royal Society of London A: Mathematical, Physical and Engineering Sciences*, 260:218–236, 1961.

[16] S. W. Van Sciver and C. F. Barenghi. Visualisation of quantum turbulence. *Progress in Low Temperature Physics*, 16:247–303, 2009.

[17] W. F. Vinen. Mutual friction in a heat current in liquid helium II. *Proceedings of the Royal Society of London A: Mathematical, Physical and Engineering Sciences*, 242:493–515, 1957.

[18] L. Skrbek and K. R. R. Sreenivasan. Developed quantum turbulence and its decay. *Physics of Fluids*, 24(1):011301, 2012.

[19] A. N. Kolmogorov. The local structure of turbulence in incompressible viscous fluid for very large Reynolds numbers. *Proceedings of the USSR Academy of Sciences*, 30(4):301–305, 1941.

[20] L. F. Richardson. Atmospheric diffusion shown on a distance-neighbour graph. *Proceedings of the Royal Society of London A: Mathematical, Physical and Engineering Sciences*, 110:709–737, 1926.

[21] J. Maurer and P. Tabeling. Local investigation of superfluid turbulence. *Europhysics Letters*, 43:29, 1998.

[22] D. Duda, P. Švančara, M. La Mantia, M. Rotter, and L. Skrbek. Visualization of viscous and quantum flows of liquid ^{4}He due to an oscillating cylinder of rectangular cross section. *Physical Review B*, 92:064519, 2015.

[23] D. R. Poole, C. F. Barenghi, Y. A. Sergeev, and W. F. Vinen. Motion of tracer particles in He II. *Physical Review B*, 71:064514, 2005.

[24] E. Fonda, D. P. Meichle, N. T. Ouellette, S. Hormoz, and D. P. Lathrop. Direct observation of Kelvin waves excited by quantized vortex reconnection. *Proceedings of the National Academy of Sciences*, 111(Suppl. 1):4707–4710, 2014.

[25] M. Raffel, Ch. E. Willert, S. Wereley, and J. Kompenhans. *Particle Image Velocimetry - A Practical Guide*. Springer-Verlag Berlin Heidelberg, 2007.

[26] W. Guo, M. La Mantia, D. P. Lathrop, and S. W. Van Sciver. Visualization of two-fluid flows of superfluid helium-4. *Proceedings of the National Academy of Sciences*, 111(Suppl. 1):4653–4658, 2014.

[27] G. Careri, S. Cunsolo, and P. Mazzoldi. Critical drift velocity of ions in liquid helium. *Physical Review Letters*, 7(5):151, 1961.

[28] W. Guo and H. J. Maris. Observations of the motion of single electrons in liquid helium. *Journal of Low Temperature Physics*, 148(3):199–206, 2007.

[29] J. Gao, A. Marakov, W. Guo, B. T. Pawlowski, S. W. Van Sciver, G. G. Ihas, D. N. McKinsey, and W. F. Vinen. Producing and imaging a thin line of He_2^* molecular tracers in helium-4. *Review of Scientific Instruments*, 86(9):093904, 2015.

[30] A. Marakov, J. Gao, W. Guo, S. W. Van Sciver, G. G. Ihas, D. N. McKinsey, and W. F. Vinen. Visualization of the normal-fluid turbulence in counterflowing superfluid ^{4}He. *Physical Review B*, 91:094503, 2015.

[31] V. Uruba. *Turbulence*. ČVUT, Prague, second edition, 2014.

[32] R. J. Donnelly, A. N. Karpetis, J. J. Niemela, K. R. Sreenivasan, W. F. Vinen, and C. M. White. The use of particle image velocimetry in the study of turbulence in liquid helium. *Journal of Low Temperature Physics*, 126(1-2):327–332, 2002.

[33] T. Zhang, D. Celik, and S. W. Van Sciver. Tracer particles for application to PIV studies of liquid helium. *Journal of Low Temperature Physics*, 134(3):985–1000, 2004.

[34] D. P. Meichle and D. P. Lathrop. Nanoparticle dispersion in superfluid helium. *Review of Scientific Instruments*, 85(7):073705, 2014.

[35] K. L. Chopra and J. B. Brown. Suspension of particles in liquid helium. *Physical Review*, 108(1):157, 1957.

[36] R. E. Boltnev, G. Frossati, E. B. Gordon, I. N. Krushinskaya, E. A. Popov, and A. Usenko. Embedding impurities into liquid helium. *Journal of Low Temperature Physics*, 127(5):245–258, 2002.

[37] M. La Mantia, T. V. Chagovets, M. Rotter, and L. Skrbek. Testing the performance of a cryogenic visualization system on thermal counterflow by using hydrogen and deuterium solid tracers. *Review of Scientific Instruments*, 83(5):055109, 2012.

[38] D. Celik and S. W. Van Sciver. Tracer particle generation in superfluid helium through cryogenic liquid injection for particle image velocimetry (PIV) applications. *Experimental Thermal and Fluid Science*, 26(8):971–975, 2002.

[39] E. Fonda, K. R. Sreenivasan, and D. P. Lathrop. Sub-micron solid air tracers for quantum vortices and liquid helium flows. *Review of Scientific Instruments*, 87(2):025106, 2016.

[40] T. Zhang and S. W. Van Sciver. Large-scale turbulent flow around a cylinder in counterflow superfluid ^{4}He (He (II)). *Nature Physics*, 1(1):36–38, 2005.

[41] M. Murakami and N. Ichikawa. Flow visualization study of thermal counterflow jet in He II. *Cryogenics*, 29(4):438–443, 1989.

[42] M. Bourgoin, J.-F. Pinton, and R. Volk. *Modeling Atmospheric and Oceanic Flows: Insights from Laboratory Experiments and Numerical Simulations*, chapter Lagrangian Methods in Experimental Fluid Mechanics, pages 277–296. John Wiley & Sons, Inc., Hoboken, 2014.

[43] A. F. Trotman-Dickenson and J. C. Bailar. *Comprehensive inorganic chemistry: H, noble gases, group IA, group IIA, group IIIB, C and Si*, volume 1. Pergamon, Oxford, 1973.

[44] I. F. Sbalzarini and P. Koumoutsakos. Feature point tracking and trajectory analysis for video imaging in cell biology. *Journal of Structural Biology*, 151(2):182–195, 2005.

[45] W. F. Vinen and L. Skrbek. Quantum turbulence generated by oscillating structures. *Proceedings of the National Academy of Sciences*, 111(Suppl. 1):4699–4706, 2014.

[46] M. La Mantia and L. Skrbek. Quantum, or classical turbulence? *Europhysics Letters*, 105(4):46002, 2014.

[47] S. Babuin, E. Varga, L. Skrbek, E. Lévêque, and P.-E. Roche. Effective viscosity in quantum turbulence: A steady-state approach. *Europhysics Letters*, 106(2):24006, 2014.

[48] N. Mordant, E. Lévêque, and J.-F. Pinton. Experimental and numerical study of the Lagrangian dynamics of high Reynolds turbulence. *New Journal of Physics*, 6(1):116, 2004.

[49] M. S. Paoletti, M. E. Fisher, K. R. Sreenivasan, and D. P. Lathrop. Velocity statistics distinguish quantum turbulence from classical turbulence. *Phys. Rev. Lett.*, 101:154501, 2008.

[50] I. P. D. De Silva and H. J. S. Fernando. Oscillating grids as a source of nearly isotropic turbulence. *Physics of Fluids*, 6(7):2455–2464, 1994.

[51] R. E. Honey, R. Hershberger, R. J. Donnelly, and D. Bolster. Oscillating-grid experiments in water and superfluid helium. *Physical Review E*, 89(5):053016, 2014.

[52] N. F. Sy, M. Bourgoin, P. Diribarne, M. Gibert, and B. Rousset. Oscillating grid high Reynolds experiments in superfluid. In B. J. Boersma, W.-P. Breugem, G. E. Elsinga, R. Pecnik, C. Poelma, and J. Westerweel, editors, *Proceedings of the 15th European Turbulence Conference*, page 318. Delft University of Technology, 2015.

[53] S. I. Davis, P. C. Hendry, and P. V. E. McClintock. Decay of quantized vorticity in superfluiduid 4-He at mK temperatures. *Physica B*, 280:43–44, 2000.

[54] G. A. Voth, A. La Porta, A. M. Crawford, J. Alexander, and E. Bodenschatz. Measurement of particle accelerations in fully developed turbulence. *Journal of Fluid Mechanics*, 469:121–160, 2002.

[55] N. Mordant, P. Metz, O. Michel, and J.-F. Pinton. Measurement of Lagrangian velocity in fully developed turbulence. *Physical Review Letters*, 87(21):214501, 2001.

[56] N. Mordant, A. M. Crawford, and E. Bodenschatz. Three-dimensional structure of the Lagrangian acceleration in turbulent flows. *Physical Review Letters*, 93(21):214501, 2004.

[57] M. La Mantia, D. Duda, M. Rotter, and L. Skrbek. Lagrangian accelerations of particles in superfluid turbulence. *Journal of Fluid Mechanics*, 717, 2013.

[58] E. Lévêque and A. Naso. Introduction of longitudinal and transverse Lagrangian velocity increments in homogeneous and isotropic turbulence. *Europhysics Letters*, 108(5):54004, 2014.

[59] N. T. Ouellette, H. Xu, M. Bourgoin, and E. Bodenschatz. An experimental study of turbulent relative dispersion models. *New Journal of Physics*, 8(6):109, 2006.

Attachments

[A1] M. La Mantia, P. Švančara, D. Duda and L. Skrbek. Small-scale universality of particle dynamics in quantum turbulence, *Physical Review B*, 94:184512, 2016.

[A2] Abstract for the International Conference on Quantum Fluids and Solids 2016, August 11-16, 2016, Prague [accepted for poster presentation]

[A3] Abstract for the 11$^{\text{th}}$ European Fluid Mechanics Conference, September 12-16, 2016, Seville [accepted for oral presentation]

[A4] Abstract for the conference Topical Problems of Fluid Mechanics, February 15-17, 2017, Prague [accepted for oral presentation]